Allosteric activation or inhibition of PI3Kγ mediated through conformational changes in the p110γ helical domain

Noah J Harris[1*], Meredith L Jenkins[1*], Sung-Eun Nam[2] Manoj K Rathinaswamy[1], Matthew AH Parson[1], Harish Ranga-Prasad[1], Udit Dalwadi[2], Brandon E Moeller[1], Eleanor Sheekey[1], Scott D Hansen[3], Calvin K Yip[2%], and John E Burke[1,2%]

[1]Department of Biochemistry and Microbiology, University of Victoria, Victoria, British Columbia, V8W 2Y2, Canada

[2]Department of Biochemistry and Molecular Biology, The University of British Columbia, Vancouver, British Columbia V6T 1Z3, Canada

[3]Department of Chemistry and Biochemistry, Institute of Molecular Biology, University of Oregon, Eugene, OR 97403

*These authors contributed equally

[%]To whom correspondence should be addressed: John E. Burke

Tel: 1-250-721-8732, email: jeburke@uvic.ca

Calvin K. Yip

Tel: 1-604-827-3976, email: calvin.yip@ubc.ca

Keywords: PI3K, PIK3CG, PI3Kγ, p110γ, p101, p84, PIK3R5, PIK3R6, phosphoinositide 3-kinase, hydrogen exchange, protein kinase C, PKC, nanobodies.

Abstract

PI3Kγ is a critical immune signaling enzyme activated downstream of diverse cell surface molecules, including Ras, PKCβ activated by the IgE receptor, and Gβγ subunits released from activated GPCRs. PI3Kγ can form two distinct complexes, with the p110γ catalytic subunit binding to either a p101 or p84 regulatory subunit, with these complexes being differentially activated by upstream stimuli. Here using a combination of Cryo electron microscopy, HDX-MS, and biochemical assays we have identified novel roles of the helical domain of p110γ in regulating lipid kinase activity of distinct PI3Kγ complexes. We defined the molecular basis for how an allosteric inhibitory nanobody potently inhibits kinase activity through rigidifying the helical domain and regulatory motif of the kinase domain. The nanobody did not block either p110γ membrane recruitment or Ras/Gβγ binding, but instead decreased ATP turnover. We also identified that p110γ can be activated by dual PKCβ helical domain phosphorylation leading to partial unfolding of an N-terminal region of the helical domain. PKCβ phosphorylation is selective for p110γ-p84 compared to p110γ-p101, driven by differential dynamics of the helical domain of these different complexes. Nanobody binding prevented PKCβ mediated phosphorylation. Overall, this works shows an unexpected allosteric regulatory role of the helical domain of p110γ that is distinct between p110γ-p84 and p110γ-p101, and reveals how this can be modulated by either phosphorylation or allosteric inhibitory binding partners. This opens possibilities of future allosteric inhibitor development for therapeutic intervention.

Introduction

The class I phosphoinositide 3 kinases (PI3Ks) are master regulators of myriad functions through their generation of the lipid signalling molecule phosphatidylinositol 3,4,5-trisphosphate (PIP_3) downstream of cell surface receptors (Burke and Williams, 2015; Rathinaswamy and Burke, 2019; Vanhaesebroeck et al., 2021; Vasan and Cantley, 2022). The class I PI3Ks can be further subdivided into the class IA and class IB subfamilies, with class IB PI3Ks being critical in immune signalling, and are composed of a single p110γ catalytic subunit that can bind to either a p101 or p84 regulatory subunit (Hawkins and Stephens, 2015; Lanahan et al., 2022; Okkenhaug, 2013). The two PI3Kγ complexes (either p110γ-p84 or p110γ-p101) play essential and independent roles in both the adaptative and innate immune systems. PI3Kγ has shown promise as a therapeutic target, primarily as an immunomodulator of the tumor microenvironment leading to enhanced anti-tumor immune responses (De Henau et al., 2016; Kaneda et al., 2016b). Multiple isoform selective small molecule ATP competitive inhibitors of p110γ are in clinical trials for multiple forms of human cancers (Li et al., 2021). However, all inhibitors currently developed towards p110γ act as ATP competitive inhibitors, showing equal potency against both p110γ-p84 or p110γ-p101 complexes.

Detailed experiments on the role of p110γ in mice show that knockout of both p101 and p84 leads to PIP_3 levels that are equivalent to knockout of p110γ, showing that all cellular PI3Kγ activity requires the presence of either a p84 or p101 regulatory subunit (Rynkiewicz et al., 2020). The two complexes are differentially activated by membrane localised receptors, including G-protein coupled receptors (Li et al., 2000; Stephens et al., 1997), Ras (Jin et al., 2020; Kurig et al., 2009), toll like receptors (TLRs) (Luo et al., 2018), and the IgE antigen receptor (Laffargue et al., 2002; Walser et al., 2013). This leads to the different complexes driving unique immune responses, with p110γ-p101involved in chemotaxis in neutrophils (Bohnacker et al., 2009; Deladeriere et al., 2015), and p110γ-p84 involved in reactive oxide production. Differential activation of unique PI3Kγ complexes downstream of GPCRs and Ras is caused by the ability of p101 to directly bind to Gβγ subunits downstream of activated GPCRs, with this being lost in

p84, making p110γ-p84 activation by Gβγ dependent on Ras mediated membrane recruitment (Rathinaswamy et al., 2023; Kurig et al., 2009; Rynkiewicz et al., 2020). Activation of PI3Kγ downstream of the IgE antigen receptor is driven by calcium mediated activation of protein kinase Cβ, leading to the selective phosphorylation and activation of p110γ at S582 (Walser et al., 2013), with this putatively only occurring in p110γ-p84 and not p110γ-p101. The full molecular mechanisms underlying how phosphorylation of p110γ is selective for different p84 or p101 complexes, and how it activates lipid kinase activity are poorly understood.

Extensive biophysical approaches including cryo electron microscopy (cryo-EM), X-ray crystallography, and hydrogen deuterium exchange mass spectrometry (HDX-MS) have provided extensive insight into the molecular underpinnings of how p110γ associates with both p101 and p84, how they are differentially activated by Ras and GPCR signals, and how they can be activated on lipid membranes (Pacold et al., 2000; Walker et al., 1999; Rathinaswamy et al., 2021c, 2021a; Gangadhara et al., 2019; Vadas et al., 2013; Rathinaswamy et al., 2023). The p110γ catalytic subunit is composed of an adaptor binding domain (ABD), a Ras binding domain (RBD), a C2 domain, a helical domain, and a bi-lobal kinase domain (Rathinaswamy et al., 2021a; Walker et al., 1999). A set of helices positioned C-terminal to the activation loop in the kinase domain play a critical role in regulating activity, with this region referred to as the regulatory motif (Rathinaswamy et al., 2021c). The p110γ isoform is unique in that it is inhibited in the absence of a regulatory subunit, with this driven by an autoinhibitory conformation of the regulatory motif, that is proposed to require membrane association to disrupt (Gangadhara et al., 2019). The regulatory motif is a common site of activating mutations in the other class I PI3K isoforms (Jenkins et al., 2023), with p110γ having rare activating oncogenic mutants in this region (Rathinaswamy et al., 2021c). The p110γ subunit interacts with both p84 and p101 at an interface composed of the C2 domain, and the linkers between the RBD-C2 and C2-helical domains (Rathinaswamy et al., 2023, 2021a). The p110γ-p84 complex forms a more dynamic complex compared to p110γ-p101 (Rathinaswamy et al., 2023; Shymanets et al., 2013), however, no clear unique regulatory role of this difference in dynamics has been identified.

The fundamental roles of p110γ in inflammatory processes has made it a therapeutic target in many pathological conditions, including asthma (Campa et al., 2018), arthritis (Camps et al., 2005), obesity (Becattini et al., 2011; Breasson et al., 2017), and cancer (De Henau et al., 2016; Kaneda et al., 2016a, 2016b). There are significant side effects from non-isoform selective PI3K inhibitors (Bohnacker et al., 2017; Vanhaesebroeck et al., 2021), which has driven the development of highly p110γ selective small molecule inhibitors (Bell et al., 2012; Evans et al., 2016; Gangadhara et al., 2019). However, all p110γ inhibitors will target both p110γ-p101 and p110γ-p84, so there is a potential for the development of allosteric inhibitors outside of the ATP binding site. Initial promise has been reported for the development of class IA p110α oncogene specific allosteric inhibitors. However, further investigation of the molecular mechanisms underlying p110γ regulation will be required for the discovery of regions that can be targeted for allosteric inhibitor development.

Here we report critical roles of the helical domain of p110γ in both activation and inhibition of lipid kinase activity. We characterised an allosteric inhibitory nanobody (NB7) that potently inhibits p110γ activity. Cryo-EM was used to define the inhibitory interface, which is composed of the helical domain, the ABD-RBD linker, and the regulatory motif of the kinase domain of p110γ. The region that the nanobody binds to is in close spatial proximity to a previously identified PKCβ phosphorylation site (S582) in the helical domain, and oncogenic activating mutants in the regulatory motif. We fully characterised the activity and dynamics of stoichiometrically PKCβ phosphorylated p110γ, leading to the discovery of a novel additional phosphorylation site (S594/S595). PKCβ phosphorylation was highly selective for p110γ and p110γ-p84, with limited phosphorylation of p110γ-p101. Hydrogen deuterium exchange mass spectrometry (HDX-MS) analysis showed that phosphorylation of p110γ leads to unfolding of the N-terminal region of the helical domain, and increased kinase activity. The presence of the inhibitory nanobody significantly blocks PKCβ phosphorylation, with phosphorylated p110γ showing no detectable binding to NB7. Overall, this work provides unique insight into the critical role of the helical domain in controlling p110γ activity, and how

140 phosphorylation and binding partners can modify this regulation. It also reveals a unique
141 binding site located at the interface of the helical and kinase domain that can be targeted
142 for future allosteric inhibitor design.
143
144 **Results**
145 *Molecular mechanism of nanobody inhibition of p110γ*
146 We previously identified multiple nanobodies that inhibited the activity of p110γ.
147 One from this group (denoted NB7 throughout the manuscript) potently inhibited the
148 membrane mediated activation of p110γ-p84 by both Ras and Gβγ, with HDX-MS
149 experiments mapping the NB7 binding interface to the RBD, helical and kinase domains
150 (Rathinaswamy et al., 2021b). We originally hypothesized that NB7 worked by sterically
151 inhibiting Ras binding to the RBD domain of p110γ. To further explore the molecular
152 mechanism of inhibition we purified all complexes of p110γ (p110γ apo, p110γ-p84,
153 p110γ-p101) along with the NB7 nanobody. The SDS-PAGE of all proteins utilised in this
154 study are shown in the source data file included in the supplemental information.
155 To define the mechanism concerning how NB7 inhibits PI3K activity we analyzed
156 how this nanobody inhibited all class IB PI3K complexes (p110γ, p110γ-p84, p110γ-p101)
157 upon activation by lipidated Gβγ subunits. Intriguingly, we found that all three forms of
158 p110γ were potently inhibited by NB7 (Fig. 1A). While the IC_{50} measured for the three
159 complexes was different, this is likely mainly due to the dramatic difference in protein
160 required to measure lipid kinase activity *in vitro* (~300 nM for p110γ apo/p110γ-p84, and
161 ~10 nM for p110γ-p101, respectively). This suggested that the mechanism of inhibition
162 was not driven by a steric block of Ras association through the RBD, as previously
163 proposed (Rathinaswamy et al., 2021b). We examined the binding of this nanobody to all
164 complexes using biolayer interferometry (BLI). The nanobody bound equivalently tightly
165 to all complexes, with ~2 nM potency for p110γ, p110γ-p84, and p110γ-p101 (Fig. 1B).
166 We also tested binding of the nanobody to all class IA PI3Ks, and there was no detectable
167 binding to p110α, p110β, and p110δ (Fig. 1C).

To further understand the mechanism by which this nanobody blocked lipid kinase activity we measured the bulk membrane recruitment dynamics of fluorescently labeled Dy647-p84-p110γ on supported lipid bilayers (SLBs) using Total Internal Reflection Fluorescence (TIRF) Microscopy. We found that the nanobody had no effect on membrane recruitment of p110γ-p84 on bilayers containing membrane-tethered Ras(GTP) and Gβγ (Fig. 1D-F). Membrane binding was not affected when the nanobody was spiked into samples containing membrane associated Dy647-p84-p110γ (Fig 1D). Similarly, pre-incubation of Dy647-p84-p110γ with 500 nM NB7 did not perturb membrane association of the kinase when flowed over a supported membrane (Fig. 1E).

We wanted to define the molecular mechanism of how nanobody NB7 was a potent allosteric inhibitor of lipid kinase activity. We purified the complex of nanobody NB7 bound to p110γ-p84 to homogeneity by gel filtration. Using this sample, we obtained a cryo-EM reconstruction of the complex of nanobody (NB7)-bound p110γ at 3.0-Å overall resolution from 149,603 particles (Figs. 2A-D, S1 and supplemental table 1). The density map was of sufficient quality to perform automated and manual construction of the p110γ-NB7 complex, with unambiguous building of the interfacial contacts between NB7 and p110γ. Nanobody binding did not induce any large-scale conformational changes of p110γ, as the structure of p110γ bound to NB7 was similar to the apo p110γ crystal structure or p110γ-p101 cryo-EM structure (Fig. S2). The lowest local resolution was in the ABD domain, with increased B-factors of the ABD in the p110γ-NB7 structure compared to p110γ-p101 (Fig. S2). This is consistent with the concept that ABD flexibility plays an important role in class I PI3K regulation (Liu et al., 2022).

The interface between NB7 and p110γ was extensive, with ~1200 Å of buried surface area, with interactions of the ABD-RBD linker, N-terminus of the helical domain, and the regulatory motif at the turn between kα8-kα9 (1022-1026aa). This location in the regulatory motif is where both activating oncogenic (R1021C) and inhibitory loss of function mutants have been identified (R1021P) (Takeda et al., 2019), as well as a putative inhibitory phosphorylation site (T1024) (Perino et al., 2011). The resolution was sufficient to unambiguous build the three complementarity determining region (CDR)

loops of NB7 that mediate target selectivity (Fig. 2E-F). The interface is primarily hydrophobic, with only 8 hydrogen bonds, and 1 electrostatic interaction among the 33 interfacial residues of NB7. A pocket formed between the helical domain and the ABD-RBD linker forms the majority of the interface, with extensive interactions with the long CDR3. The CDR1 loop packed up against the N-terminal section of the helical domain, with the CDR2 loop forming the interface with the regulatory motif. Previous study of oncogenic mutants in the regulatory motif of p110γ showed that increased dynamics mediated by these mutants increased kinase activity, putatively by breaking the autoinhibitory tryptophan lock in kα12 of the regulatory motif. Therefore, rigidifying the regulatory motif likely explains the molecular basis for how it prevents kinase activity. The nanobody interface is distinct from the predicted Gβγ interface (Rathinaswamy et al., 2023) and the experimentally resolved Ras interface (Pacold et al., 2000), explaining why it can still be membrane recruited by these stimuli.

p110γ activation by helical domain phosphorylation

To further understand the potential role helical domain dynamics in regulating p110γ activity we searched for any possible regulatory roles of this in PI3K signalling. It has been previously identified that p110γ is directly phosphorylated by the protein kinase PKCβ on residue S582 in the helical domain (Walser et al., 2013). S582 is located on the interior of the helical domain, and would not be expected to be exposed when the N-terminal region of the helical domain is folded (Fig. 3A). To understand this better at a molecular level, we purified a catalytic fragment of PKCβ and performed protein phosphorylation reactions on p110γ apo, p110γ-p84, and p110γ-p101. We identified a phosphorylated peptide containing S582, and surprisingly, we found an additional p110γ phosphorylation site at S594/S595 (Fig. 3B, Fig. S3). The S594/S595 site is also located in the N-terminal region of the helical domain, and is even more buried than S582, and would not be expected to be exposed when this region is folded (Fig. 3A). Dose response curves of PKCβ treatment were carried out for p110γ (Fig. 3C), p110γ-p84 (Fig. 3D), and p110γ-p101 (Fig. 3E). Both p110γ and p110γ-p84 showed similar dose response curves

for PKCβ treatment, with similar curves for S582 and S594/S595. The p110γ-p101 complex was only very weakly phosphorylated, with <100-fold lower levels compared to p110γ and p110γ-p84 (Fig. 3E). This is consistent with the helical domain in p110γ being more rigid when bound to p101, compared to either bound to p84 or p110γ alone.

To provide additional insight into the molecular mechanisms underlying p110γ phosphorylation we carried out hydrogen deuterium exchange mass spectrometry (HDX-MS) experiments on p110γ and phosphorylated p110γ (90.8% phosphorylated S594/595, 92% phosphorylated S582) (Fig. 4A). The full data underlying the experiment is available in the source data, and data processing information is in supplemental table 2. We have previously observed that the N-terminal region of the helical domain of apo p110γ (residues spanning 557-630aa) shows isotope profiles that are consistent with EX1 H/D exchange kinetics (Rathinaswamy et al., 2021b, 2021c; Vadas et al., 2013; Walser et al., 2013). This is indicative of cooperative unfolding of extended protein regions, with H/D exchange occurring faster than the refolding event. This region is where the PKC phosphorylation sites are located, and may explain how the buried residues S582 and S594/S595 can be exposed to PKC. This is compatible with the observation that p110γ-p101 is protected from phosphorylation, as it does not show EX1 kinetics in this region, whereas both p110γ and p110γ-p84 do (Rathinaswamy et al., 2021a).

When we compared phosphorylated p110γ (>90.8% as measured by mass spectrometry at both sites) to unphosphorylated p110γ we observed extensive increases in dynamics in the C2, helical domain and kinase domain (Fig. 4A-D). The largest increases in exchange upon phosphorylation were located in the N-terminal region of the helical domain, with the peptides directly adjacent to the phosphorylation site showing almost complete deuterium incorporation at the earliest time points of exchange. This is indicative of significant disruption of the alpha helical secondary structure in this region. When we examined the exchange profiles in this region they still underwent EX1 kinetics (Fig. 4C), however, phosphorylated p110γ was enriched in the more fully deuterated species. In addition to the regions in the helical domain, a portion of the regulatory motif of the kinase domain also showed increased deuterium exposure. This included the kα9-

kα12 helices that surround the activation loop of p110γ. These increases in exchange were similar to those we had observed in a R1021C oncogenic activating mutant of *PIK3CG* (Rathinaswamy et al., 2021c).

To further explore the potential role of phosphorylation in mediating p110γ activity, we examined the kinase activity of p110γ for both basal ATPase and lipid membranes. Assays measured the hydrolysis of ATP to ADP, with this acting as a surrogate for PIP_3 production in the membrane assay. PKCβ-mediated phosphorylation enhanced the ATPase activity of p110γ ~2-fold in both the absence and presence of membranes (Fig. 4E).

Nanobody blocks p110γ phosphorylation

As NB7 bound at the interface of the helical and kinase domains that is exposed upon PKC phosphorylation of p110γ we hypothesized that the nanobody would likely alter phosphorylation. We carried out PKC phosphorylation of p110γ, p110γ-p101 and p110γ bound to NB7. The presence of NB7 showed even lower phosphorylation than p110γ-p101, with almost complete abrogation of phosphorylation at both sites (Fig. 5A-B). We also wanted to determine whether p110γ phosphorylation reciprocally perturbed NB7 binding. BLI experiments showed that there was no detectable binding of NB7 to phosphorylated p110γ (Fig. 5C-D), consistent with phosphorylation disrupting the N-terminal region of the p110γ helical domain. In addition, lipid kinase assays using phosphorylated p110γ showed no detectable difference in activity when measured in the absence and presence nanobody (Fig. 5E).

Discussion

Here we find that the helical domain is a central regulator of the p110γ catalytic subunit of class IB PI3K, with modulation of helical dynamics through binding partners or PTMs able to either increase or decrease lipid kinase activity. These results expand on previous work defining the helical domain as a central regulator of class IA PI3Ks, where the nSH2 domain of the p85 regulatory subunits makes inhibitory interactions that

significantly inhibit lipid kinase activity of all class IA catalytic subunits (p110α, p110β, and p110δ) (Mandelker et al., 2009; Miled et al., 2007; Burke and Williams, 2013; Burke, 2018). This inhibitory interaction in class IA PI3Ks is disrupted in human cancers (helical hotspot mutations in *PIK3CA*) (Samuels et al., 2004) and immune disorders (helical mutations in *PIK3CD* in APDS1) (Angulo et al., 2013; Lucas et al., 2014). Class IB PI3Ks are unique compared to class IA PI3Ks, as they are not inhibited by p101 and p84 regulatory subunits, but instead potentiate GPCR activation. This lack of inhibition is due to the distinct binding interface of class IB PI3K regulatory subunits compared to class IA regulatory subunits, with only class IA regulatory subunits making direct inhibitory interactions with the kinase and helical domains of p110 catalytic subunits (Rathinaswamy et al., 2021a). Here we show that a unique surface at the interface of the helical and kinase domains of p110γ is a potential site for the development of novel allosteric inhibitors that modulate p110γ activity.

The previously identified inhibitory nanobody (NB7) (Rathinaswamy et al., 2021b) bound with high affinity and inhibited all complexes of p110γ. The nanobody interface is distinct from how the nSH2 inhibits class IA PI3K activity, as its binding site is on the opposite face of the helical domain (Fig. 6A). The mechanism of inhibition is also distinct, as the nSH2-helical interaction plays a critical role in preventing membrane recruitment of inhibited class I PI3Ks, with removal of this interface either through pYXXM motif binding, or oncogenic mutations leading to increased membrane recruitment (Burke et al., 2012, 2011; Zhang et al., 2011). Analysis of the nanobody binding site compared to the structure of HRas-p110γ or the HDX-MS supported Alphafold-multimer prediction of Gβγ-p110γ (Rathinaswamy et al., 2023) shows that nanobody binding does not sterically block complex formation (Fig. 6B). This is consistent with it not blocking membrane recruitment by Ras/Gβγ.The nanobody inhibited ATP turnover both in solution and on membranes, suggesting that it prevents formation of a catalytically competent conformation of p110γ, but still allows for membrane recruitment. Further development of small molecule allosteric binding partners in this allosteric pocket between the kinase and helical domain may reveal the specific molecular interactions in this pocket that mediate inhibition.

Oncogenic mutations are frequent in the class IA PI3Kα encoded by *PIK3CA*, with this being the 2nd most frequently mutated gene in human cancer (Lawrence et al., 2014). Mutations in p110γ encoded by *PIK3CG* in cancer are less frequent, however, they can still provide insight into regulatory mechanisms that control activity. Oncogenic mutations in the kinase domain (R1021C) and helical domain (E581K) are in close proximity to the nanobody binding site, and both would be expected to disrupt the stability of the helical domain or regulatory motif of the kinase domain (Fig. 6C). In addition to these mutations there are also multiple post-translational modifications that occur in this region, including inhibitory phosphorylation at T1024 (Perino et al., 2011), and activating phosphorylation at S582 (Walser et al., 2013). PKCβ is activated downstream of the IgE receptor in mast cells (Walser et al., 2013), but the full details of how this activates PI3K has been unclear. We identified an additional PKCβ phosphorylation site located in the helical domain (S594/S595) (Fig. 6C). Both the S582 and S594/S595 sites are not surface accessible and would require a transient opening of the helical domain for kinase accessibility. HDX-MS analysis of the helical domain of p110γ has shown that it is more dynamic than other class I PI3K isoforms (Burke and Williams, 2013; Walser et al., 2013), with the presence of the p101 regulatory subunit dramatically decreasing helical domain dynamics (Vadas et al., 2013). This putative mechanism of helical domain dynamics driving PKCβ phosphorylation is consistent with our observation that p101 subunits decreased p110γ phosphorylation >100-fold. PKCβ phosphorylation of p110γ leads to increased dynamics in both the helical and kinase domains with increased kinase activity, although only weakly compared to full activation by either membrane localised Ras or Gβγ. This increase was observed with both membrane and soluble substrate, so likely is not driven by altered membrane recruitment.

Overall, our biophysical and biochemical analysis of modulators of helical domain dynamics reveal the critical role of this domain in regulating class IB PI3K activity. This raises possibilities for development of small molecule modulators that may either increase or decrease helical domain dynamics, leading to either activation or inhibition. The high-resolution structure of an allosteric inhibitor nanobody provide initial insight into which pockets can specifically be targeted. Multiple ATP competitive p110γ selective inhibitors

344 are in clinical trials for human cancers (Li et al., 2021), with many having significant side
345 effects. The identification of novel inhibitory strategies provides new opportunities for
346 targeting p110γ dysregulation in human disease.
347
348 **Acknowledgements**
349 J.E.B. is supported by the Canadian Institute of Health Research (CIHR, 168998),
350 and the Michael Smith Foundation for Health Research (MSFHR, scholar 17686). C.K.Y.
351 is supported by CIHR (FDN-143228, PJT-168907) and the Natural Sciences and
352 Engineering Research Council of Canada (RGPIN-2018-03951). S.D.H. is supported by
353 an NSF CAREER Award (MCB-2048060). This research project was supported in part by
354 the UBC High Resolution Macromolecular Cryo-Electron Microscopy Facility (HRMEM).
355 A portion of this research was supported by NIH grant U24GM129547 and performed at
356 the PNCC at OHSU and accessed through EMSL (grid.436923.9), a DOE Office of
357 Science User Facility sponsored by the Office of Biological and Environmental Research.
358 We appreciate help from Theo Humphreys and Rose Marie Haynes with data collection
359 at PNCC. Competing Interests: The authors declare that they have no competing
360 interests.
361
362 **Conflict of Interest statement**
363 JEB reports personal fees from Scorpion Therapeutics, Reactive therapeutics and
364 Olema Oncology; and research grants from Novartis. Other authors declare no competing
365 interests.
366
367 **Methods**

Resources table	SOURCE	IDENTIFIER
Bacterial and virus strains		
E.coli XL10-GOLD KanR Ultracompetent Cells	Agilent	200317
E.coli DH10EMBacY Competent Cells	Geneva Biotech	DH10EMBacY
Chemicals, peptides, and recombinant proteins		
Deuterium Oxide 99.9%	Sigma	151882
Guanosine 5′-diphosphate (GDP) sodium salt hydrate	Sigma	G7127-100MG
Guanosine 5′-triphosphate (GTP) sodium salt hydrate	Sigma	G8877-250MG
Sodium deoxycholate	Sigma	D6750

Polyoxyethylene (10) lauryl ether	Sigma	P9769
CHAPS, Molecular Biology Grade	EMD Millipore	220201
Phosphatidylserine (Porcine Brain)	Avanti	840032C
Phosphatidylethanolamine (Egg yolk)	Sigma	P6386
Cholesterol	Sigma	47127-U
Phosphatidylcholine (Egg yolk)	Avanti	840051C
Phosphatidylinositol-4,5-bisphosphate (Porcine Brain)	Avanti	840046
Sphingomyelin (Egg yolk)	Sigma	S0756
1,2-dioleoyl-sn-glycero-3-phosphocholine (DOPC)	Avanti	850375C
1,2-dioleoyl-*sn*-glycero-3-phospho-L-serine (18:1, DOPS)	Avanti	840035C
1,2-dioleoyl-sn-glycero-3-phosphoethanolamine-N-[4-(p-maleimidomethyl)cyclohexane-carboxamide] (18:1 MCC-PE)	Avanti	780201C
10 mg/mL beta casein solution	ThermoFisher	37528
10x PBS [pH 7.4]	Corning	46-013-CM
glucose oxidase from *Aspergillus niger* (225 U/mg)	Biophoretics	B01357.02
catalase	Sigma	C40-100MG Bovine Liver
Trolox	Cayman Chemicals	10011659
Dyomics 647 maleimide dye	Dyomics	647P1-03
Coenzyme A	Sigma	C3019
Sulfuric acid	Sigma	58105-2.5L-PC
C-Flat 2/2-T grids	FisherScientific	50-192-8327
Critical commercial assays		
Transcreener ADP2 FI Assay (1,000 Assay, 384 Well)	BellBrook Labs	3013-1K
Deposited data		
PDB coordinate file for p110γ-NB7 structure	PDB	8DP0
EM density file for p110γ-NB7 complex	EMD	EMD-27627
HDX-MS and phosphorylation proteomics data	PRIDE	PXD040765
Oligonucleotides		
Fwd primer for amplifying KD of PKCβII GTATTTTCAGGGCgccggtaccACGACCAACACTGTCTCCAAATTTG	Sigma	MR51F
Rvs primer for amplifying KD of PKCβII gactcgagcggccgcTTATAGCTCTTGACTTCGGGTTTTAAAAATTCAG	Sigma	MR51R
Fwd primer for amplifying N term of PKCβII CCATCACggatctggcggtagtATGGCTGACCCGGCTGCG	Sigma	MR52F
Rvs primer for amplifying N term of PKCβII GCCCTGAAAATACAGGTTTTCCTTTTCTTCCGGGACCTTGGTTCCC	Sigma	MR52R
Fwd primer for adding stop codon to PKCβII AGTCAAGAGCTAAgcggccgctcgagtctagagcctgc	Sigma	MR56F
Rvs primer for adding stop codon to PKCβII gactcgagcggccgcTTAGCTCTTGACTTCGGGTTTTAAAAATTCAG	Sigma	MR56R
Recombinant DNA		
pMultiBac-Gβ1/Gγ2	PMID:34452907	pOP737

pACEBac1-hsp110γ	PMID:34452907	MR30
pMultiBac-hsp110γ-ssp101	PMID:34452907	MR22
pMultiBac-hsp110γ-mmp84	PMID:34452907	MR24
pFastBac HRas G12V	PMID:34452907	BS9
biGBac hsp110γ/ybbr-hsp84	PMID:36842083	HP28
biGBac hsp110γ/ybbr-hsp101	PMID:36842083	HP29
his6-GST-PrescissionProtease-SNAP-RBD(K65E)	PMID:34452907	pSH936
his6TEV-HRas(1-184aa) C118S, C181S	PMID:34452907	pSH414
his6-Gγ2, SNAP-Gβ1 (DUAL FastBac)	PMID:34452907	pSH651
pACEBAC-PKCβII (internal tev cleavage site)	This paper	pMR56
pFASTBac p110α	PMID: 28515318	pOV1181
pFASTBac p110β	PMID: 28515318	pOV1182
pFASTBac p110δ	PMID: 28515318	pOV1183
pFASTBac p85β	This paper	EX21
Software and algorithms		
COOT-0.9.4.1	CCP4	https://www2.mrc-lmb.cam.ac.uk/personal/pemsley/coot/
Phenix-1.19.1	Open source	https://www.phenix-online.org/
PDBePISA (Proteins, Interfaces, Structures and Assemblies)	EMBL-EBI	https://www.ebi.ac.uk/pdbe/pisa/pistart.html
ESPript 3.0	Robert et al NAR 2014	https://espript.ibcp.fr
HDExaminer	Sierra Analytics	http://massspec.com/hdexaminer
GraphPad Prism 7	GraphPad	https://www.graphpad.com
PyMOL	Schroedinger	http://pymol.org
Compass Data Analysis	Bruker	https://www.bruker.com
ChimeraX	UCSF	https://www.rbvi.ucsf.edu/chimerax/
ImageJ/Fiji	ImageJ	https://imagej.net/software/fiji/
Nikon NIS elements	Nikon	https://www.microscope.healthcare.nikon.com/products/software/nis-elements
cryoSPARC v.3.3.2	Structura Biotechnology	https://cryosparc.com/
Other		
Sf9 insect cells for expression	Expression Systems	94-001S
Insect cell media	Expression Systems	96-001-01
Hellmanex III cleaning solution	Fisher	14-385-864
6-well sticky-side chamber	IBIDI	80608

368

Plasmid Generation

Plasmids encoding Homo sapiens p110γ (human), Mus musculus p84 (mouse), Sus scrofa p101 (porcine), and Gβγ were used as previously described (Rathinaswamy et al., 2023, 2021a). The class IA plasmids were also used as previously described (Dornan et al., 2017; Siempelkamp et al., 2017). The pDONR223-PRKCB2 (PKCβII, uniprot identifier: P05771-2) was a gift from William Hahn & David Root (Addgene plasmid #23746; http://n2t.net/addgene: 23746; RRID:Addgene_23746) (Johannessen et al., 2010). The PKCβII construct contains an internal TEV site that cleaves the catalytic domains from the C1/C2 regulatory domains (TEV site inserted between residues 320 and 321 of PRKCB, uniprot identifier: P05771-2) and it was subcloned into a pACEBAC Sf9 expression vector for protein purification. For purification, a 10× histidine tag, a 2× strep tag, and a tobacco etch virus protease cleavage site were cloned to the N terminus of the regulatory subunits for the complex and to p110γ and PKCβII for constructs without regulatory subunits. Full details of the plasmids are included in the resource table.

Virus Generation and Amplification:

The plasmids encoding genes for insect cell expression were transformed into DH10MultiBac cells (MultiBac, Geneva Biotech) to generate baculovirus plasmid (bacmid) containing the genes of interest. Successful generation was identified by blue-white colony screening and the bacmid was purified using a standard isopropanol-ethanol extraction method. Bacteria were grown overnight (16 hours) in 3-5 mL 2xYT (BioBasic #SD7019). Cells were spun down and the pellet was resuspended in 300 µL of 50 mM Tris-HCl, pH 8.0, 10 mM EDTA, 100 mg/mL RNase A. The pellet was lysed by the addition of 300 µL of 1% sodium dodecyl sulfate (SDS) (W/V), 200 mM NaOH, and the reaction was neutralized by addition of 400 µL of 3.0 M potassium acetate, pH 5.5. Following centrifugation at 21130 RCF and 4 °C (Rotor #5424 R), the supernatant was mixed with 800 µL isopropanol to precipitate bacmid DNA. Following centrifugation, the pelleted bacmid DNA was washed with 500 µL 70% Ethanol three times. The pellet was then air dried for 1 minute and re-suspended in 50 µL Buffer EB (10 mM Tris-Cl, pH 8.5; All buffers

399 from QIAprep Spin Miniprep Kit, Qiagen #27104). Purified bacmid was then transfected
400 into Sf9 cells. 2 mL of Sf9 cells at 0.6X106 cells/mL were aliquoted into a 6-well plate and
401 allowed to attach to form a confluent layer. Transfection reactions were prepared mixing
402 8-12 µg of bacmid DNA in 100 µL 1xPBS and 12 µg polyethyleneimine
403 (Polyethyleneimine "Max" MW 40.000, Polysciences #24765, USA) in 100 µL 1xPBS and
404 the reaction was allowed to proceed for 20-30 minutes before addition to an Sf9
405 monolayer containing well. Transfections were allowed to proceed for 5-6 days before
406 harvesting virus containing supernatant as a P1 viral stock.
407 Viral stocks were further amplified by adding P1 to Sf9 cells at ~2x10^6 cells/mL
408 (2/100 volume ratio). This amplification was allowed to proceed for 4-5 days and resulted
409 in a P2 stage viral stock that was used in final protein expression. Harvesting of P2 viral
410 stocks was carried out by centrifuging cell suspensions in 50 mL Falcon tubes at 2281
411 RCF (Beckman GS-15). To the supernatant containing virus, 5-10% inactivated fetal
412 bovine serum (FBS; VWR Canada #97068-085) was added and the stock was stored at
413 4°C.
414
415 *Expression and purification of PI3Kγ, PI3Kα/β/δ and PKCβ constructs:*
416 PI3Kγ *and PKC*β constructs were expressed in Sf9 insect cells using the baculovirus
417 expression system. Following 55 hours of expression, cells were harvested by
418 centrifuging at 1680 RCF (Eppendorf Centrifuge 5810 R) and the pellets were snap-
419 frozen in liquid nitrogen. The complex was purified through a combination of nickel affinity,
420 streptavidin affinity and size exclusion chromatographic techniques.
421 Frozen insect cell pellets were resuspended in lysis buffer (20 mM Tris pH 8.0, 100
422 mM NaCl, 10 mM imidazole pH 8.0, 5% glycerol (v/v), 2 mM βME), protease inhibitor
423 (Protease Inhibitor Cocktail Set III, Sigma)) and sonicated for 2 minutes (15s on, 15s off,
424 level 4.0, Misonix sonicator 3000). Triton-X was added to the lysate to a final
425 concentration of 0.1% and clarified by spinning at 15,000 RCF at 4°C for 45 minutes
426 (Beckman Coulter JA-20 rotor). The supernatant was loaded onto a 5 mL HisTrap™ FF
427 crude column (GE Healthcare) equilibrated in NiNTA A buffer (20 mM Tris pH 8.0, 100
428 mM NaCl, 20 mM imidazole pH 8.0, 5% (v/v) glycerol, 2 mM βME). The column was

washed with high salt NiNTA A buffer (20 mM Tris pH 8.0, 1 M NaCl, 20 mM imidazole pH 8.0, 5% (v/v) glycerol, 2 mM βME), NiNTA A buffer, 6% NiNTA B buffer (20 mM Tris pH 8.0, 100 mM NaCl, 250 mM imidazole pH 8.0, 5% (v/v) glycerol, 2 mM βME) and the protein was eluted with 100% NiNTA B. The eluent was loaded onto a 5 mL StrepTrap™ HP column (GE Healthcare) equilibrated in gel filtration buffer (20mM Tris pH 8.5, 100 mM NaCl, 50 mM Ammonium Sulfate and 0.5 mM TCEP). To purify *PI3Kα/β/δ*, the purification protocol was performed as described above but instead the protein was eluted in PI3Ka gel filtration buffer (20mM HEPES 7.5, 150mM NaCl, 0.5mM TCEP). The column was washed with the corresponding gel filtration buffer and loaded with tobacco etch virus protease. After cleavage on the column overnight, the PI3Kγ protein constructs were eluted in gel filtration buffer. The protein was concentrated in a 50,000 MWCO Amicon Concentrator (Millipore) to <1 mL and injected onto a Superdex™ 200 10/300 GL Increase size-exclusion column (GE Healthcare) equilibrated in gel filtration buffer. After size exclusion, the protein was concentrated, aliquoted, frozen, and stored at -80°C. For PKCβ, the protein was eluted from the strep column in gel filtration buffer, and the eluate was then loaded on a 1ml HisTrap™ FF column to remove the his tagged LipTev. The flowthrough was collected, and the column was washed with 2ml of gel filtration buffer. These fractions were pooled and concentrated and stored at -80°C.

To purify phosphorylated p110γ, the purification protocol as described above was performed but PKCβ was added to the strep column at a molar ratio of 1:3 (PKCβII:p110) along with LipTEV, 20 mM $MgCl_2$ and 1mM ATP and allowed to incubate on ice for 4 hours. The protein was eluted by adding 7 ml of gel filtration buffer and treated with a second dose of PKCβ (same ratio as above) and allowed to incubate on ice for another 3 hours. For non-phosphorylated p110, same protocol was followed with the exception in the addition of PKCβ. Both the proteins were concentrated in a 50,000 MWCO Amicon Concentrator (Millipore) to <1 mL and injected onto a Superdex™ 200 10/300 GL Increase size-exclusion column (GE Healthcare) equilibrated in gel filtration buffer. The final phosphorylation level of the two sites was characterised by mass spectrometry, with these values being 92% and 90.8%, for S582 and S594/S595 respectively. After size exclusion, the protein was concentrated, aliquoted, frozen, and stored at -80°C.

Expression and Purification of lipidated Gβγ for kinase activity assays:

Full length, lipidated human *Gβγ* (Gβ1γ2) was expressed in Sf9 insect cells and purified as described previously. After 65 hours of expression, cells were harvested, and the pellets were frozen as described above. Pellets were resuspended in lysis buffer (20 mM HEPES pH 7.7, 100 mM NaCl, 10 mM βME, protease inhibitor (Protease Inhibitor Cocktail Set III, Sigma)) and sonicated for 2 minutes (15s on, 15s off, level 4.0, Misonix sonicator 3000). The lysate was spun at 500 RCF (Eppendorf Centrifuge 5810 R) to remove intact cells and the supernatant was centrifuged again at 25,000 RCF for 1 hour (Beckman Coulter JA-20 rotor). The pellet was resuspended in lysis buffer and sodium cholate was added to a final concentration of 1% and stirred at 4°C for 1 hour. The membrane extract was clarified by spinning at 10,000 RCF for 30 minutes (Beckman Coulter JA-20 rotor). The supernatant was diluted 3 times with NiNTA A buffer (20 mM HEPES pH 7.7, 100 mM NaCl, 10 mM Imidazole, 0.1% C12E10, 10mM βME) and loaded onto a 5 mL HisTrap™ FF crude column (GE Healthcare) equilibrated in the same buffer. The column was washed with NiNTA A, 6% NiNTA B buffer (20 mM HEPES pH 7.7, 25 mM NaCl, 250 mM imidazole pH 8.0, 0.1% C12E10, 10 mM βME) and the protein was eluted with 100% NiNTA B. The eluent was loaded onto HiTrap™ Q HP anion exchange column equilibrated in Hep A buffer (20 mM Tris pH 8.0, 8 mM CHAPS, 2 mM Dithiothreitol (DTT)). A gradient was started with Hep B buffer (20 mM Tris pH 8.0, 500 mM NaCl, 8 mM CHAPS, 2 mM DTT) and the protein was eluted in ~50% Hep B buffer. The eluent was concentrated in a 30,000 MWCO Amicon Concentrator (Millipore) to < 1 mL and injected onto a Superdex™ 75 10/300 GL size exclusion column (GE Healthcare) equilibrated in Gel Filtration buffer (20 mM HEPES pH 7.7, 100 mM NaCl, 10 mM CHAPS, 2 mM TCEP). Fractions containing protein were pooled, concentrated, aliquoted, frozen and stored at -80 °C.

Expression and purification of nanobody:

Nanobody NB7-PIK3CG with a C-terminal 6X His tag was expressed from a pMESy4 vector in the periplasm of WK6 *E.coli*. A 1L culture was grown to OD600 of 0.7

in Terrific Broth containing 0.1% glucose and 2mM MgCl2 in the presence of 100 µg/mL ampicillin and was induced with 0.5 mM isopropyl-β-D-thiogalactoside (IPTG). Cells were harvested the following day by centrifuging at 2500 RCF (Eppendorf Centrifuge 5810 R) and the pellet was snap-frozen in liquid nitrogen. The frozen pellet was resuspended in 15 mL of TES buffer containing 200 mM Tris pH 8.0, 0.5mM ethylenediaminetetraacetic acid (EDTA) and 500 mM Sucrose and was mixed for 45 minutes at 4°C. To this mixture, 30 mL of TES buffer diluted four times in water was added and mixed for 45 minutes at 4°C to induce osmotic shock. The lysate was clarified by centrifuging at 14,000 rpm for 15 minutes (Beckman Coulter JA-20 rotor). Imidazole was added to the supernatant to final concentration of 10mM loaded onto a 5 mL HisTrap™ FF crude column (GE Healthcare) equilibrated in NiNTA A buffer (20 mM Tris pH 8.0, 100 mM NaCl, 20 mM imidazole pH 8.0, 5% (v/v) glycerol, 2 mM β-mercaptoethanol (βME)). The column was washed with high salt NiNTA A buffer (20 mM Tris pH 8.0, 1 M NaCl, 20 mM imidazole pH 8.0, 5% (v/v) glycerol, 2 mM βME), followed by 100% NiNTA A buffer, then a 6% NiNTA B wash buffer (20 mM Tris pH 8.0, 100 mM NaCl, 250 mM imidazole pH 8.0, 5% (v/v) glycerol, 2 mM βME) and the protein was eluted with 100% NiNTA B. The eluent was concentrated in a 10,000 MWCO Amicon Concentrator (Millipore) to <1 mL and injected onto a Superdex™ 75 10/300 GL Increase size-exclusion column (GE Healthcare) equilibrated in gel filtration buffer (20mM Tris pH 8.5, 100 mM NaCl, 50 mM Ammonium Sulfate and 0.5 mM tris(2-carboxyethyl) phosphine (TCEP)). Following size exclusion, the protein was concentrated, frozen and stored at -80°C.

Phosphorylation analysis

For the dose–response phosphorylation of p110γ, p110/p84, and p110/p101, each protein or complex (750nM) was mixed with ATP (200 μM), GFB (20mM Tris pH 8.5, 100 mM NaCl, 50 mM Ammonium Sulfate and 0.5 mM TCEP), $MgCl_2$(20mM) and various amounts of PKC (4 µg, 800 ng, 160 ng, 32 ng, 6.4 ng, and 0 ng). Reactions were incubated for three hours on ice and quenched with 50 μL of ice-cold acidic quench buffer (0.7 M guanidine-HCl, 1% formic acid). followed by immediate freezing using liquid nitrogen and storage at –80 °C.

For the experiment studying the effect of nanobody on phosphorylation, p110γ or p110/p101, (500nM) was mixed with ATP (1 mM), GFB (20mM Tris pH 8.5, 100 mM NaCl, 50 mM Ammonium Sulfate and 0.5 mM TCEP), $MgCl_2$(20mM), with nanobody and PKC present at 1200 nM and 500nM, respectively. Reactions were incubated for one hour at room temperature and quenched with 54 μL of ice-cold acidic quench buffer (0.7 M guanidine-HCl, 1% formic acid) followed by immediate freezing using liquid nitrogen and storage at –80 °C.

Phosphorylation of all proteins was confirmed using Mass spectrometry and PEAKS7 analysis. The phosphorylated and non-phosphorylated peptide ratios were determined by generating extracted ion chromatograms for each peptide using their molecular formula and charge state in the Bruker Compass Data Analysis software. The area under each extracted curve was then extracted. The full MS quantification of each of the phosphorylated and non-phosphorylated peptide is provided in the source data.

Lipid vesicle preparation for kinase activity assays

Lipid vesicles containing 5% brain phosphatidylinositol 4,5- bisphosphate (PIP2), and 95% brain phosphatidylserine (PS), were prepared by mixing the lipids solutions in organic solvent. The solvent was evaporated in a stream of argon following which the lipid film was desiccated in a vacuum for 45 minutes. The lipids were resuspended in lipid buffer (20 mM HEPES pH 7.0, 100 mM NaCl and 10 % glycerol) and the solution was vortexed for 5 minutes followed by sonication for 15 minutes. The vesicles were then subjected to ten freeze thaw cycles and extruded 11 times through a 100-nm filter (T&T Scientific: TT-002-0010). The extruded vesicles were sub-aliquoted and stored at -80°C. Final vesicle concentration was 2 mg/mL.

Kinase Assays

All kinase assays were done using Transcreener ADP2 Fluorescence Intensity (FI) assays (Bellbrook labs) which measures ADP production. All assays used super-lipid vesicles [5% phosphatidylinositol 4,5-bisphosphate (PI(4,5)P2), and 95%

549 phosphatidylserine (PS)] at final concentration of 0.5 mg/mL, and ATP at a final
550 concentration of 100 µM.

551 For assays measuring the inhibition by nanobody, 4X kinase (final concentration:
552 330 nM for p110γ, 300nM for p110γ/p84 and 12nM for p110γ/p101) was mixed with
553 varying 4X concentrations of nanobody (final concentration: 2µM – 2.7nM) or kinase
554 buffer (20mM HEPES pH 7.5, 100mM NaCl, 3mM $MgCl_2$, 0.03% CHAPS, 2mM TCEP,
555 and 1mM EGTA) and allowed to sit on ice for 15 minutes. 2 µl of protein mix was mixed
556 with 2 µl of lipid solution containing Gβγ (1µM final concentration), ATP (100 µM), Super
557 lipid (0.5mg/ml final concentration), and lipid buffer (25mM HEPES pH 7, 5% Glycerol,
558 and 100mM NaCl) and incubated at room temperature for 60 minutes.
559 For assays comparing the difference in activation between phosphorylated and non-
560 phosphorylated p110γ, 2X kinase (final concentrations: 1µM – 12.3nM) was mixed with
561 2X lipid solutions containing ATP (100 µM), and lipid buffer and either nanobody (3 µM
562 final concentration), Super lipid (0.5mg/ml final concentration) or both nanobody and lipid.
563 The reaction was incubated at room temperature for 60 minutes.

564 After the 60-minute incubation, all reactions were stopped with 4 µL of 2X stop and
565 detect solution containing Stop and Detect buffer (20mM HEPES,0.02% Brij-35, 400mM
566 40mM EDTA pH 7.5), 8 nM ADP Alexa Fluor 594 Tracer and 93.7 µg/mL ADP2 Antibody
567 IRDye QC-1, covered and incubated at room temperature for 1 hr before reading the
568 fluorescence. The fluorescence intensity was measured using a SpectraMax M5 plate
569 reader at excitation 590 nm and emission 620 nm. All data was normalized against the
570 appropriate measurements obtained for 100 µM ATP and 100 µM ADP with no kinase.
571 The percent ATP turnover was interpolated using a standard curve (0.1-100 µM ADP).
572 Interpolated values were then used to calculate the specific activity of the enzyme.
573

574 *Biolayer interferometry*
575 All Biolayer interferometry experiments were performed using the Octet K2 (Fortebio Inc.).
576 When comparing nanobody binding to each complex, His-tagged nanobody was
577 immobilized on an Anti-Penta-His biosensor for 600s, and the sensor was dipped into
578 solutions of varying concentrations of p110γ, p110p84, and p110p101 (50 nM – 1.9 nM)

for 600s followed by a 1200s dissociation step in Octet Buffer (20 mM tris pH 8.5, 100 mM NaCl, 50 mM ammonium sulfate, 0.1% bovine serum albumin, and 0.02% Tween 20). Experiments comparing class IA PI3K versus class IB PI3K used 500 nM nanobody loaded on the Octet tip, and 50 nM of PI3Ks. When comparing nanobody binding to phosphorylated and unphosphorylated p110γ, His-tagged nanobody was immobilized on an Anti-Penta-His biosensor for 600 s, and the sensor was dipped into solutions of either phosphorylated or non-phosphorylated p110γ at a final concentration of 25 nM for 600s followed by a dissociation step for 600s. The average K_D (dissociation constant) was calculated from the binding curves based on their global fit to a 1:1 binding model.

Supported lipid bilayer TIRF microscopy experiments

The membrane binding dynamics of Dy647-p84-p110γ were measured in the absence and presence of nanobody 7 (NB7) using TIRF microscopy. As previously described (Rathinaswamy et al., 2023), supported lipid bilayers were formed using 50 nm extruded small unilamellar vesicles (SUVs) containing the following lipids: 1,2-dioleoyl-sn-glycero-3-phosphocholine (18:1 DOPC, Avanti # 850375C), 1,2-dioleoyl-*sn*-glycero-3-phospho-L-serine (18:1 DOPS, Avanti # 840035C), 1,2-dioleoyl-sn-glycero-3-phosphoethanolamine-N-[4-(p-maleimidomethyl)cyclohexane-carboxamide] (18:1 MCC-PE, Avanti # 780201C). Lipid compositions reported in figure legends represent the molar percentage of each lipid species.

To create SLBs, a total concentration of 0.25 mM lipids was solvated in 1x PBS [pH 7.4] and deposited on Piranha etched glass coverslips (25 x 75 mm) adhered to an IBIDI chamber. After a 30-minute incubation, membranes were washed with 4 mL of 1x PBS [pH 7.4] and then blocked for 10 minutes with 1 mg/mL beta casein (Thermo FisherSci, Cat# 37528) in 1x PBS [pH 7.4] (Corning, Cat# 46-013-CM). To conjugate H-Ras to maleimide lipids (MCC-PE), blocked membranes were incubated with 30 μM H-Ras(GDP) in buffer containing 1x PBS [pH 7.4], 1 mM $MgCl_2$, 50 μM GDP, and 0.1 mM TCEP for 2 hours. The membrane conjugation reaction was terminated after 2 hours with 1x PBS [pH 7.4] containing 5 mM β-mercaptoethanol (βME). Membranes were then

608 washed and stored in 1x PBS [pH 7.4] until performing the TIRF-M membrane binding
609 experiments. H-Ras was purified as previously described (Rathinaswamy et al., 2023).
610 To perform the TIRF-M membrane binding assays, 200 nM farnesyl-$G\beta\gamma$ was
611 equilibrated into the supported membranes for 30 minutes. In parallel, nucleotide
612 exchange of H-Ras(GDP) was performed by adding 50 nM guanine nucleotide exchange
613 factor (SosCat) in 1x PBS [pH 7.4], 1 mM $MgCl_2$, 50 μM GDP. To measure membrane
614 binding, Dy647-p84-p110γ was diluted into the following buffer: 20 mM HEPES [pH 7.0],
615 150 mM NaCl, 50 μM GTP, 1 mM ATP, 5 mM $MgCl_2$, 0.5 mM EGTA, 20 mM glucose, 200
616 μg/mL beta casein (ThermoScientific, Cat# 37528), 20 mM BME, 320 μg/mL glucose
617 oxidase (Serva, #22780.01 *Aspergillus niger*), 50 μg/mL catalase (Sigma, #C40-100MG
618 Bovine Liver), and 2 mM Trolox. Trolox was prepared as previously described (Hansen
619 et al., 2019). Perishable reagents (i.e. glucose oxidase, catalase, and Trolox) were added
620 10 minutes before image acquisition.
621 TIRF-M experiments were performed using an inverted Nikon Ti2 microscope with
622 a 100x Nikon (1.49 NA) oil immersion objective. The x-axis and y-axis positions were
623 controlled using a Nikon motorized stage. Dy647-p84-p110γ was excited with a 637 nm
624 diode laser (OBIS laser diode, Coherent Inc. Santa Clara, CA) controlled with an acousto-
625 optic tunable filter (AOTF) and laser launch built by Vortran (Sacramento, CA). The power
626 output measured through the objective for single particle imaging was 1-3 mW. Excitation
627 light passing through quad multi-pass dichroic filter cube (Semrock). Fluorescence
628 emission passed through Nikon emission filter wheel containing the following 25 mm
629 ET700/75M emission filters (Semrock) before being detected on iXion Life 897 EMCCD
630 camera (Andor Technology Ltd., UK). All TIRF-M experiments were performed at room
631 temperature (23ºC). Microscope hardware was controlled using Nikon NIS elements.
632 Data analysis was performed using ImageJ/Fiji and Prism graphing program.
633
634 *Cryo-EM Sample Preparation and Data Collection*
635 3 μL of purified nanobody-bound p110γ at 0.45 mg/ml was adsorbed onto C-Flat 2/2-T
636 grids that were glow discharged for 25 s at 15 mA. Grids were then plunged into liquid
637 ethane using a Vitrobot Mark IV (Thermo Fisher Scientific) with the following settings: -5

638 blot force, 1.5 s blot time, 100% humidity and 4 °C. Vitrified specimens were screened for
639 ice and particle quality at the UBC High resolution macromolecular electron microscopy
640 (HRMEM) facility using a 200-kV Glacios transmission electron microscope equipped with
641 a Falcon 3EC direct electron detector (DED). Clipped grids were sent to the Pacific
642 Northwest Cryo-EM Center (PNCC) where 7,322 movies were collected using a Titan
643 Krios equipped with a Gatan K3 DED and a BioQuantum K3 energy filter with a slit width
644 of 20 eV. The movies were collected at a physical pixel size of 0.830 Å/pix and a total
645 dose of 50e^-/Å^2 over 50 frames.

646

647 *Cryo-EM image analysis*

648 The data were processed using cryoSPARC v.3.3.2 (Punjani et al., 2017). The
649 movies were pre-processed by patch motion correction using default settings except
650 Fourier-cropping by a factor of 2, followed by patch CTF estimation using default settings.
651 A 3D map of PI3K p110γ-p101 complex (EMD-23808) was used to create 2D projections
652 for use as templates to auto-pick 1,463,553 particles. Particles were extracted with a box
653 size of 380 pixels, Fourier cropped to a box size of 96 pixels and subjected to 2D
654 classification. After discarding classes with obvious noise and no features, 795,162
655 particles were used for multiple rounds of *ab initio* reconstruction and heterogeneous
656 refinement using 4 or 5 classes. 365,178 particles, which generated the two best 3D
657 reconstruction, were used to carry out Per-particle local-motion correction with 760 pixels
658 box size later downsized to 380 pixels followed by several rounds of *ab initio*
659 reconstruction and heterogeneous refinement using 3 or 5 classes. 149,603 from best
660 class were further refined by homogeneous refinement and a final Non-Uniform (NU)-
661 refinement which generated a reconstruction with an overall resolution of 3.02 Å based
662 on the Fourier shell correlation (FSC) 0.143 criterion.

663

664 *Building the structural model of p110γ-NB7*

665 The previous structural model of full length p110γ from the complex of p110γ-
666 p101(PDB: 7MEZ) (Rathinaswamy et al., 2021a) was fit into the map using Chimera

(Pettersen et al., 2004). A model of the nanobody was generated using Alphafold2 using the Colabfold v1.5.2 server (Mirdita et al., 2022). The CDR loops were removed from this initial model, and the remaining nanobody was fit into the map using Chimera. The final structure was built by iterative rounds of automated model building in Phenix, manual model building in COOT (Emsley et al., 2010), and refinement in Phenix.real_space_refine using realspace, rigid body, and adp refinement with tight secondary structure restraints (Afonine et al., 2012). This allowed for unambiguous building of the CDRs of the nanobody, and their interface with p110γ. The full refinement and validation statistics are shown in Supplemental table 1.

Hydrogen Deuterium eXchange Mass Spectrometry

Exchange reactions to assess differences in p110γ upon phosphorylation were carried out at 20°C in 10 μL volumes with final concentrations of 1.6 μM for both apo and phosphorylated p110γ. A total of two conditions were assessed: p110γ apo and PKCβ phosphorylated p110γ. The hydrogen-deuterium exchange reaction was initiated by the addition of 8 μL D_2O buffer (94.3% D_2O, 100 mM NaCl, 20 mM HEPES pH 7.5) to the 2 μL protein for a final D_2O concentration of 75.4%. Exchange was carried out over five time points (3s on ice, and 3s, 30s, 300s and 3000s at 20°C) and the reaction was quenched with addition of 60 μL of ice-cold acidic quench buffer (0.7 M guanidine-HCl, 1% formic acid). After quenching, samples were immediately frozen in liquid nitrogen and stored at -80°C. All reactions were carried out in triplicate.

Protein Digestion and MS/MS Data Collection: Protein samples were rapidly thawed and injected onto an integrated fluidics system containing a HDx-3 PAL liquid handling robot and climate-controlled chromatography system (LEAP Technologies), a Dionex Ultimate 3000 UHPLC system, as well as an Impact HD QTOF Mass spectrometer (Bruker). The protein was run over two immobilized pepsin columns (Applied Biosystems; Poroszyme™ Immobilized Pepsin Cartridge, 2.1 mm x 30 mm; Thermo-Fisher 2-3131-00; at 10°C and 2°C respectively) at 200 µL/min for 3 minutes. The resulting peptides were collected and desalted on a C18 trap column [Acquity UPLC BEH C18 1.7 mm

column (2.1 x 5 mm); Waters 186003975]. The trap was subsequently eluted in line with an ACQUITY 1.7 μm particle, 100 x 1 mm2 C18 UPLC column (Waters 186002352), using a gradient of 3-35% B (buffer A, 0.1% formic acid; buffer B, 100% acetonitrile) over 11 min immediately followed by a gradient of 35-80% B over 5 minutes. MS experiments acquired over a mass range from 150 to 2200 mass/charge ratio (m/z) using an electrospray ionization source operated at a temperature of 200°C and a spray voltage of 4.5 kV.

Peptide Identification: Peptides were identified using data-dependent acquisition following tandem MS/MS experiments (0.5 s precursor scan from 150-2000 m/z; twelve 0.25 s fragment scans from 150-2000 m/z). MS/MS datasets were analyzed using PEAKS7 (PEAKS), and a false discovery rate was set at 0.1% using a database of purified proteins and known contaminants. Same approach was used to identify phosphorylated and non-phosphorylated peptides for our in-vitro phosphorylation experiments, with variable phosphorylation of STY residues was added to the search. The search parameters were set with a precursor tolerance of 20 parts per million, fragment mass error 0.02 Da, and charge states from 1 to 8, with a selection criterion of peptides that had a −10logP score of >24.03 for phosphorylated and >23.05 for non-phosphorylated. The MS/MS spectra of the PKC phosphorylated peptides are included in Fig S3.

Mass Analysis of Peptide Centroids and Measurement of Deuterium Incorporation: HD-Examiner Software (Sierra Analytics) was used to automatically calculate the level of deuterium incorporation into each peptide. All peptides were manually inspected for correct charge state, correct retention time, and appropriate selection of isotopic distribution. Deuteration levels were calculated using the centroid of the experimental isotope clusters. HDX-MS results are presented with no correction for back exchange shown in the Source data, with the only correction being applied correcting for the deuterium oxide percentage of the buffer used in the exchange (75.4%). Changes in any peptide at any time point greater than specified cut-offs (5% and 0.45 Da) and with an unpaired, two-tailed t-test value of $p<0.01$ was considered significant. A number of

peptides in the helical domain showed isotope distributions consistent with EX1 H/D exchange. Attempts to define the relative percentages of each population using HDExaminer were extremely noisy, so representative EX1 profiles are shown in Fig. 3C. The raw peptide deuterium incorporation graphs for a selection of peptides with significant differences are shown in Fig. 4D, with the raw data for all analysed peptides in the source data. To allow for visualization of differences across all peptides, we utilized number of deuteron difference (#D) plots (Fig. 4B). These plots show the total difference in deuterium incorporation over the entire H/D exchange time course, with each point indicating a single peptide. The data analysis statistics for all HDX-MS experiments are in Supplemental Table 2 according to the guidelines of (Masson et al., 2019). The mass spectrometry proteomics data have been deposited to the ProteomeXchange Consortium via the PRIDE partner repository (Perez-Riverol et al., 2022) with the dataset identifier PXD040765.

References

Afonine PV, Grosse-Kunstleve RW, Echols N, Headd JJ, Moriarty NW, Mustyakimov M, Terwilliger TC, Urzhumtsev A, Zwart PH, Adams PD. 2012. Towards automated crystallographic structure refinement with phenix.refine. *Acta Crystallogr D Biol Crystallogr* **68**:352–367. doi:10.1107/S0907444912001308

Angulo I, Vadas O, Garçon F, Banham-Hall E, Plagnol V, Leahy TR, Baxendale H, Coulter T, Curtis J, Wu C, Blake-Palmer K, Perisic O, Smyth D, Maes M, Fiddler C, Juss J, Cilliers D, Markelj G, Chandra A, Farmer G, Kielkowska A, Clark J, Kracker S, Debré M, Picard C, Pellier I, Jabado N, Morris JA, Barcenas-Morales G, Fischer A, Stephens L, Hawkins P, Barrett JC, Abinun M, Clatworthy M, Durandy A, Doffinger R, Chilvers ER, Cant AJ, Kumararatne D, Okkenhaug K, Williams RL, Condliffe A, Nejentsev S. 2013. Phosphoinositide 3-kinase δ gene mutation predisposes to respiratory infection and airway damage. *Science* **342**:866–871. doi:10.1126/science.1243292

Becattini B, Marone R, Zani F, Arsenijevic D, Seydoux J, Montani J, Dulloo A, Thorens B, Preitner F, Wymann M, Solinas G. 2011. PI3Kgamma within a nonhematopoietic cell type negatively regulates diet-induced thermogenesis and promotes obesity and insulin resistance. *Proc Natl Acad Sci USA* **108**:E854-63. doi:10.1073/pnas.1106698108/-/DCSupplemental

Bell K, Sunose M, Ellard K, Cansfield A, Taylor J, Miller W, Ramsden N, Bergamini G, Neubauer G. 2012. SAR studies around a series of triazolopyridines as potent and selective PI3Kγ inhibitors. *Bioorg Med Chem Lett* **22**:5257–5263. doi:10.1016/j.bmcl.2012.06.049

764 Bohnacker T, Marone R, Collmann E, Calvez R, Hirsch E, Wymann M. 2009.
765 PI3Kgamma adaptor subunits define coupling to degranulation and cell motility
766 by distinct PtdIns(3,4,5)P3 pools in mast cells. *Sci Signal* **2**:ra27.
767 doi:10.1126/scisignal.2000259
768 Bohnacker T, Prota AE, Beaufils F, Burke JE, Melone A, Inglis AJ, Rageot D, Sele AM,
769 Cmiljanovic V, Cmiljanovic N, Bargsten K, Aher A, Akhmanova A, Díaz JF,
770 Fabbro D, Zvelebil M, Williams RL, Steinmetz MO, Wymann MP. 2017.
771 Deconvolution of Buparlisib's mechanism of action defines specific PI3K and
772 tubulin inhibitors for therapeutic intervention. *Nat Commun* **8**:14683.
773 doi:10.1038/ncomms14683
774 Breasson L, Becattini B, Sardi C, Molinaro A, Zani F, Marone R, Botindari F,
775 Bousquenaud M, Ruegg C, Wymann MP, Solinas G. 2017. PI3Kγ activity in
776 leukocytes promotes adipose tissue inflammation and early-onset insulin
777 resistance during obesity. *Sci Signal* **10**:eaaf2969. doi:10.1126/scisignal.aaf2969
778 Burke JE. 2018. Structural Basis for Regulation of Phosphoinositide Kinases and Their
779 Involvement in Human Disease. *Mol Cell* **71**:653–673.
780 doi:10.1016/j.molcel.2018.08.005
781 Burke JE, Perisic O, Masson GR, Vadas O, Williams RL. 2012. Oncogenic mutations
782 mimic and enhance dynamic events in the natural activation of phosphoinositide
783 3-kinase p110α (PIK3CA). *Proc Natl Acad Sci USA* **109**:15259–15264.
784 doi:10.1073/pnas.1205508109
785 Burke JE, Vadas O, Berndt A, Finegan T, Perisic O, Williams RL. 2011. Dynamics of the
786 phosphoinositide 3-kinase p110δ interaction with p85α and membranes reveals
787 aspects of regulation distinct from p110α. *Structure* **19**:1127–1137.
788 doi:10.1016/j.str.2011.06.003
789 Burke JE, Williams RL. 2015. Synergy in activating class I PI3Ks. *Trends in Biochemical*
790 *Sciences* **40**:88–100. doi:10.1016/j.tibs.2014.12.003
791 Burke JE, Williams RL. 2013. Dynamic steps in receptor tyrosine kinase mediated
792 activation of class IA phosphoinositide 3-kinases (PI3K) captured by H/D
793 exchange (HDX-MS). *Adv Biol Regul* **53**:97–110. doi:10.1016/j.jbior.2012.09.005
794 Campa CC, Silva RL, Margaria JP, Pirali T, Mattos MS, Kraemer LR, Reis DC, Grosa
795 G, Copperi F, Dalmarco EM, Lima-Júnior RCP, Aprile S, Sala V, Dal Bello F,
796 Prado DS, Alves-Filho JC, Medana C, Cassali GD, Tron GC, Teixeira MM,
797 Ciraolo E, Russo RC, Hirsch E. 2018. Inhalation of the prodrug PI3K inhibitor
798 CL27c improves lung function in asthma and fibrosis. *Nat Commun* **9**:5232–16.
799 doi:10.1038/s41467-018-07698-6
800 Camps M, Rückle T, Ji H, Ardissone V, Rintelen F, Shaw J, Ferrandi C, Chabert C,
801 Gillieron C, Françon B, Martin T, Gretener D, Perrin D, Leroy D, Vitte P-A, Hirsch
802 E, Wymann MP, Cirillo R, Schwarz MK, Rommel C. 2005. Blockade of
803 PI3Kgamma suppresses joint inflammation and damage in mouse models of
804 rheumatoid arthritis. *Nat Med* **11**:936–943. doi:10.1038/nm1284
805 De Henau O, Rausch M, Winkler D, Campesato LF, Liu C, Cymerman DH, Budhu S,
806 Ghosh A, Pink M, Tchaicha J, Douglas M, Tibbitts T, Sharma S, Proctor J,
807 Kosmider N, White K, Stern H, Soglia J, Adams J, Palombella VJ, McGovern K,

Kutok JL, Wolchok JD, Merghoub T. 2016. Overcoming resistance to checkpoint blockade therapy by targeting PI3Kγ in myeloid cells. *Nature* **539**:443–447. doi:10.1038/nature20554

Deladeriere A, Gambardella L, Pan D, Anderson KE, Hawkins PT, Stephens LR. 2015. The regulatory subunits of PI3Kγ control distinct neutrophil responses. *Sci Signal* **8**:ra8. doi:10.1126/scisignal.2005564

Dornan GL, Siempelkamp BD, Jenkins ML, Vadas O, Lucas CL, Burke JE. 2017. Conformational disruption of PI3Kδ regulation by immunodeficiency mutations in PIK3CD and PIK3R1. *Proc Natl Acad Sci USA* **114**:1982–1987. doi:10.1073/pnas.1617244114

Emsley P, Lohkamp B, Scott WG, Cowtan K. 2010. Features and development of Coot. *Acta Crystallogr D Biol Crystallogr* **66**:486–501. doi:10.1107/S0907444910007493

Evans CA, Liu T, Lescarbeau A, Nair SJ, Grenier L, Pradeilles JA, Glenadel Q, Tibbitts T, Rowley AM, DiNitto JP, Brophy EE, O'Hearn EL, Ali JA, Winkler DG, Goldstein SI, O'Hearn P, Martin CM, Hoyt JG, Soglia JR, Cheung C, Pink MM, Proctor JL, Palombella VJ, Tremblay MR, Castro AC. 2016. Discovery of a Selective Phosphoinositide-3-Kinase (PI3K)-γ Inhibitor (IPI-549) as an Immuno-Oncology Clinical Candidate. *ACS Med Chem Lett* **7**:862–867. doi:10.1021/acsmedchemlett.6b00238

Gangadhara G, Dahl G, Bohnacker T, Rae R, Gunnarsson J, Blaho S, Öster L, Lindmark H, Karabelas K, Pemberton N, Tyrchan C, Mogemark M, Wymann MP, Williams RL, Perry MWD, Papavoine T, Petersen J. 2019. A class of highly selective inhibitors bind to an active state of PI3Kγ. *Nature Chemical Biology* **15**:348–357. doi:10.1038/s41589-018-0215-0

Hansen SD, Huang WYC, Lee YK, Bieling P, Christensen SM, Groves JT. 2019. Stochastic geometry sensing and polarization in a lipid kinase-phosphatase competitive reaction. *Proc Natl Acad Sci U S A* **116**:15013–15022. doi:10.1073/pnas.1901744116

Hawkins PT, Stephens LR. 2015. PI3K signalling in inflammation. *Biochim Biophys Acta* **1851**:882–897. doi:10.1016/j.bbalip.2014.12.006

Jenkins ML, Ranga-Prasad H, Parson MAH, Harris NJ, Rathinaswamy MK, Burke JE. 2023. Oncogenic mutations of PIK3CA lead to increased membrane recruitment driven by reorientation of the ABD, p85 and C-terminus. *Nat Commun* **14**:181. doi:10.1038/s41467-023-35789-6

Jin JR, Gogvadze E, Xavier AR, Bohnacker T, Voelzmann J, Wymann MP. 2020. PI3Kγ Regulatory Protein p84 Determines Mast Cell Sensitivity to Ras Inhibition-Moving Towards Cell Specific PI3K Targeting? *Front Immunol* **11**:585070. doi:10.3389/fimmu.2020.585070

Johannessen CM, Boehm JS, Kim SY, Thomas SR, Wardwell L, Johnson LA, Emery CM, Stransky N, Cogdill AP, Barretina J, Caponigro G, Hieronymus H, Murray RR, Salehi-Ashtiani K, Hill DE, Vidal M, Zhao JJ, Yang X, Alkan O, Kim S, Harris JL, Wilson CJ, Myer VE, Finan PM, Root DE, Roberts TM, Golub T, Flaherty KT, Dummer R, Weber BL, Sellers WR, Schlegel R, Wargo JA, Hahn WC, Garraway

LA. 2010. COT drives resistance to RAF inhibition through MAP kinase pathway reactivation. *Nature* **468**:968–972. doi:10.1038/nature09627

Kaneda MM, Cappello P, Nguyen AV, Ralainirina N, Hardamon CR, Foubert P, Schmid MC, Sun P, Mose E, Bouvet M, Lowy AM, Valasek MA, Sasik R, Novelli F, Hirsch E, Varner JA. 2016a. Macrophage PI3Kγ Drives Pancreatic Ductal Adenocarcinoma Progression. *Cancer Discov* **6**:870–885. doi:10.1158/2159-8290.CD-15-1346

Kaneda MM, Messer KS, Ralainirina N, Li H, Leem CJ, Gorjestani S, Woo G, Nguyen AV, Figueiredo CC, Foubert P, Schmid MC, Pink M, Winkler DG, Rausch M, Palombella VJ, Kutok J, McGovern K, Frazer KA, Wu X, Karin M, Sasik R, Cohen EEW, Varner JA. 2016b. PI3Kγ is a molecular switch that controls immune suppression. *Nature* **539**:437–442. doi:10.1038/nature19834

Kurig B, Shymanets A, Bohnacker T, Prajwal, Brock C, Ahmadian MR, Schaefer M, Gohla A, Harteneck C, Wymann MP, Jeanclos E, Nürnberg B. 2009. Ras is an indispensable coregulator of the class IB phosphoinositide 3-kinase p87/p110gamma. *Proc Natl Acad Sci USA* **106**:20312–20317. doi:10.1073/pnas.0905506106

Laffargue M, Calvez R, Finan P, Trifilieff A, Barbier M, Altruda F, Hirsch E, Wymann MP. 2002. Phosphoinositide 3-kinase gamma is an essential amplifier of mast cell function. *Immunity* **16**:441–451.

Lanahan SM, Wymann MP, Lucas CL. 2022. The role of PI3Kγ in the immune system: new insights and translational implications. *Nat Rev Immunol*. doi:10.1038/s41577-022-00701-8

Lawrence MS, Stojanov P, Mermel CH, Robinson JT, Garraway LA, Golub TR, Meyerson M, Gabriel SB, Lander ES, Getz G. 2014. Discovery and saturation analysis of cancer genes across 21 tumour types. *Nature* **505**:495–501. doi:10.1038/nature12912

Li H, Prever L, Hirsch E, Gulluni F. 2021. Targeting PI3K/AKT/mTOR Signaling Pathway in Breast Cancer. *Cancers (Basel)* **13**:3517. doi:10.3390/cancers13143517

Li Z, Jiang H, Xie W, Zhang Z, Smrcka AV, Wu D. 2000. Roles of PLC-beta2 and -beta3 and PI3Kgamma in chemoattractant-mediated signal transduction. *Science* **287**:1046–1049. doi:10.1126/science.287.5455.1046

Liu X, Zhou Q, Hart JR, Xu Y, Yang S, Yang D, Vogt PK, Wang M-W. 2022. Cryo-EM structures of cancer-specific helical and kinase domain mutations of PI3Kα. *Proc Natl Acad Sci U S A* **119**:e2215621119. doi:10.1073/pnas.2215621119

Lucas CL, Kuehn HS, Zhao F, Niemela JE, Deenick EK, Palendira U, Avery DT, Moens L, Cannons JL, Biancalana M, Stoddard J, Ouyang W, Frucht DM, Rao VK, Atkinson TP, Agharahimi A, Hussey AA, Folio LR, Olivier KN, Fleisher TA, Pittaluga S, Holland SM, Cohen JI, Oliveira JB, Tangye SG, Schwartzberg PL, Lenardo MJ, Uzel G. 2014. Dominant-activating germline mutations in the gene encoding the PI(3)K catalytic subunit p110δ result in T cell senescence and human immunodeficiency. *Nat Immunol* **15**:88–97. doi:10.1038/ni.2771

Luo L, Wall AA, Tong SJ, Hung Y, Xiao Z, Tarique AA, Sly PD, Fantino E, Marzolo M-P, Stow JL. 2018. TLR Crosstalk Activates LRP1 to Recruit Rab8a and PI3Kγ for

Suppression of Inflammatory Responses. *Cell Rep* **24**:3033–3044. doi:10.1016/j.celrep.2018.08.028

Mandelker D, Gabelli SB, Schmidt-Kittler O, Zhu J, Cheong I, Huang C-H, Kinzler KW, Vogelstein B, Amzel LM. 2009. A frequent kinase domain mutation that changes the interaction between PI3Kalpha and the membrane. *Proc Natl Acad Sci USA* **106**:16996–17001. doi:10.1073/pnas.0908444106

Masson GR, Burke JE, Ahn NG, Anand GS, Borchers C, Brier S, Bou-Assaf GM, Engen JR, Englander SW, Faber J, Garlish R, Griffin PR, Gross ML, Guttman M, Hamuro Y, Heck AJR, Houde D, Iacob RE, Jørgensen TJD, Kaltashov IA, Klinman JP, Konermann L, Man P, Mayne L, Pascal BD, Reichmann D, Skehel M, Snijder J, Strutzenberg TS, Underbakke ES, Wagner C, Wales TE, Walters BT, Weis DD, Wilson DJ, Wintrode PL, Zhang Z, Zheng J, Schriemer DC, Rand KD. 2019. Recommendations for performing, interpreting and reporting hydrogen deuterium exchange mass spectrometry (HDX-MS) experiments. *Nat Methods* **16**:595–602. doi:10.1038/s41592-019-0459-y

Miled N, Yan Y, Hon W-C, Perisic O, Zvelebil M, Inbar Y, Schneidman-Duhovny D, Wolfson HJ, Backer JM, Williams RL. 2007. Mechanism of two classes of cancer mutations in the phosphoinositide 3-kinase catalytic subunit. *Science* **317**:239–242. doi:10.1126/science.1135394

Mirdita M, Schütze K, Moriwaki Y, Heo L, Ovchinnikov S, Steinegger M. 2022. ColabFold: making protein folding accessible to all. *Nat Methods* **19**:679–682. doi:10.1038/s41592-022-01488-1

Okkenhaug K. 2013. Signaling by the phosphoinositide 3-kinase family in immune cells. *Annu Rev Immunol* **31**:675–704. doi:10.1146/annurev-immunol-032712-095946

Pacold ME, Suire S, Perisic O, Lara-Gonzalez S, Davis CT, Walker EH, Hawkins PT, Stephens L, Eccleston JF, Williams RL. 2000. Crystal structure and functional analysis of Ras binding to its effector phosphoinositide 3-kinase gamma. *Cell* **103**:931–943.

Perez-Riverol Y, Bai J, Bandla C, García-Seisdedos D, Hewapathirana S, Kamatchinathan S, Kundu DJ, Prakash A, Frericks-Zipper A, Eisenacher M, Walzer M, Wang S, Brazma A, Vizcaíno JA. 2022. The PRIDE database resources in 2022: a hub for mass spectrometry-based proteomics evidences. *Nucleic Acids Res* **50**:D543–D552. doi:10.1093/nar/gkab1038

Perino A, Ghigo A, Ferrero E, Morello F, Santulli G, Baillie GS, Damilano F, Dunlop AJ, Pawson C, Walser R, Levi R, Altruda F, Silengo L, Langeberg LK, Neubauer G, Heymans S, Lembo G, Wymann MP, Wetzker R, Houslay MD, Iaccarino G, Scott JD, Hirsch E. 2011. Integrating Cardiac PIP(3) and cAMP Signaling through a PKA Anchoring Function of p110gamma. *Mol Cell* **42**:84–95. doi:10.1016/j.molcel.2011.01.030

Pettersen EF, Goddard TD, Huang CC, Couch GS, Greenblatt DM, Meng EC, Ferrin TE. 2004. UCSF Chimera--a visualization system for exploratory research and analysis. *J Comput Chem* **25**:1605–1612. doi:10.1002/jcc.20084

Punjani A, Rubinstein JL, Fleet DJ, Brubaker MA. 2017. cryoSPARC: algorithms for rapid unsupervised cryo-EM structure determination. *Nat Methods* **14**:290–296. doi:10.1038/nmeth.4169

Rathinaswamy MK, Burke JE. 2019. Class I phosphoinositide 3-kinase (PI3K) regulatory subunits and their roles in signaling and disease. *Adv Biol Regul* 100657. doi:10.1016/j.jbior.2019.100657

Rathinaswamy MK, Dalwadi U, Fleming KD, Adams C, Stariha JTB, Pardon E, Baek M, Vadas O, DiMaio F, Steyaert J, Hansen SD, Yip CK, Burke JE. 2021a. Structure of the phosphoinositide 3-kinase (PI3K) p110γ-p101 complex reveals molecular mechanism of GPCR activation. *Sci Adv* **7**:eabj4282. doi:10.1126/sciadv.abj4282

Rathinaswamy MK, Fleming KD, Dalwadi U, Pardon E, Harris NJ, Yip CK, Steyaert J, Burke JE. 2021b. HDX-MS-optimized approach to characterize nanobodies as tools for biochemical and structural studies of class IB phosphoinositide 3-kinases. *Structure* **29**:1371-1381.e6. doi:10.1016/j.str.2021.07.002

Rathinaswamy MK, Gaieb Z, Fleming KD, Borsari C, Harris NJ, Moeller BE, Wymann MP, Amaro RE, Burke JE. 2021c. Disease-related mutations in PI3Kγ disrupt regulatory C-terminal dynamics and reveal a path to selective inhibitors. *Elife* **10**:e64691. doi:10.7554/eLife.64691

Rathinaswamy MK, Jenkins ML, Duewell BR, Zhang X, Harris NJ, Evans JT, Stariha JTB, Dalwadi U, Fleming KD, Ranga-Prasad H, Yip CK, Williams RL, Hansen SD, Burke JE. 2023. Molecular basis for differential activation of p101 and p84 complexes of PI3Kγ by Ras and GPCRs. *Cell Rep* **42**:112172. doi:10.1016/j.celrep.2023.112172

Rynkiewicz NK, Anderson KE, Suire S, Collins DM, Karanasios E, Vadas O, Williams R, Oxley D, Clark J, Stephens LR, Hawkins PT. 2020. Gβγ is a direct regulator of endogenous p101/p110γ and p84/p110γ PI3Kγ complexes in mouse neutrophils. *Sci Signal* **13**:eaaz4003. doi:10.1126/scisignal.aaz4003

Samuels Y, Wang Z, Bardelli A, Silliman N, Ptak J, Szabo S, Yan H, Gazdar A, Powell S, Riggins G, Willson J, Markowitz S, Kinzler K, Vogelstein B, Velculescu V. 2004. High frequency of mutations of the PIK3CA gene in human cancers. *Science* **304**:554. doi:10.1126/science.1096502

Shymanets A, Prajwal P, Bucher K, Beer-Hammer S, Harteneck C, Nürnberg B. 2013. p87 and p101 subunits are distinct regulators determining class IB PI3K specificity. *J Biol Chem* **288(43)**:31059–68. doi:10.1074/jbc.M113.508234

Siempelkamp BD, Rathinaswamy MK, Jenkins ML, Burke JE. 2017. Molecular mechanism of activation of class IA phosphoinositide 3-kinases (PI3Ks) by membrane-localized HRas. *J Biol Chem* **292**:12256–12266. doi:10.1074/jbc.M117.789263

Stephens LR, Eguinoa A, Erdjument-Bromage H, Lui M, Cooke F, Coadwell J, Smrcka AS, Thelen M, Cadwallader K, Tempst P, Hawkins PT. 1997. The Gbg sensitivity of a PI3K is dependent upon a tightly associated adaptor, p101. *Cell* **89**:105–114.

Takeda AJ, Maher TJ, Zhang Y, Lanahan SM, Bucklin ML, Compton SR, Tyler PM, Comrie WA, Matsuda M, Olivier KN, Pittaluga S, McElwee JJ, Long Priel DA, Kuhns DB, Williams RL, Mustillo PJ, Wymann MP, Koneti Rao V, Lucas CL.

2019. Human PI3Kγ deficiency and its microbiota-dependent mouse model reveal immunodeficiency and tissue immunopathology. *Nat Commun* **10**:4364–12. doi:10.1038/s41467-019-12311-5

Vadas O, Dbouk HA, Shymanets A, Perisic O, Burke JE, Abi Saab WF, Khalil BD, Harteneck C, Bresnick AR, Nürnberg B, Backer JM, Williams RL. 2013. Molecular determinants of PI3Kγ-mediated activation downstream of G-protein-coupled receptors (GPCRs). *Proc Natl Acad Sci U S A* **110**:18862–18867. doi:10.1073/pnas.1304801110

Vanhaesebroeck B, Perry MWD, Brown JR, André F, Okkenhaug K. 2021. PI3K inhibitors are finally coming of age. *Nat Rev Drug Discov* **20**:741–769. doi:10.1038/s41573-021-00209-1

Vasan N, Cantley LC. 2022. At a crossroads: how to translate the roles of PI3K in oncogenic and metabolic signalling into improvements in cancer therapy. *Nat Rev Clin Oncol*. doi:10.1038/s41571-022-00633-1

Walker EH, Perisic O, Ried C, Stephens L, Williams RL. 1999. Structural insights into phosphoinositide 3-kinase catalysis and signalling. *Nature* **402**:313–320. doi:10.1038/46319

Walser R, Burke JE, Gogvadze E, Bohnacker T, Zhang X, Hess D, Küenzi P, Leitges M, Hirsch E, Williams RL, Laffargue M, Wymann MP. 2013. PKCβ phosphorylates PI3Kγ to activate it and release it from GPCR control. *PLoS Biol* **11**:e1001587. doi:10.1371/journal.pbio.1001587

Zhang X, Vadas O, Perisic O, Anderson KE, Clark J, Hawkins PT, Stephens LR, Williams RL. 2011. Structure of lipid kinase p110β/p85β elucidates an unusual SH2-domain-mediated inhibitory mechanism. *Mol Cell* **41**:567–578. doi:10.1016/j.molcel.2011.01.026

Figures and Figure Legends

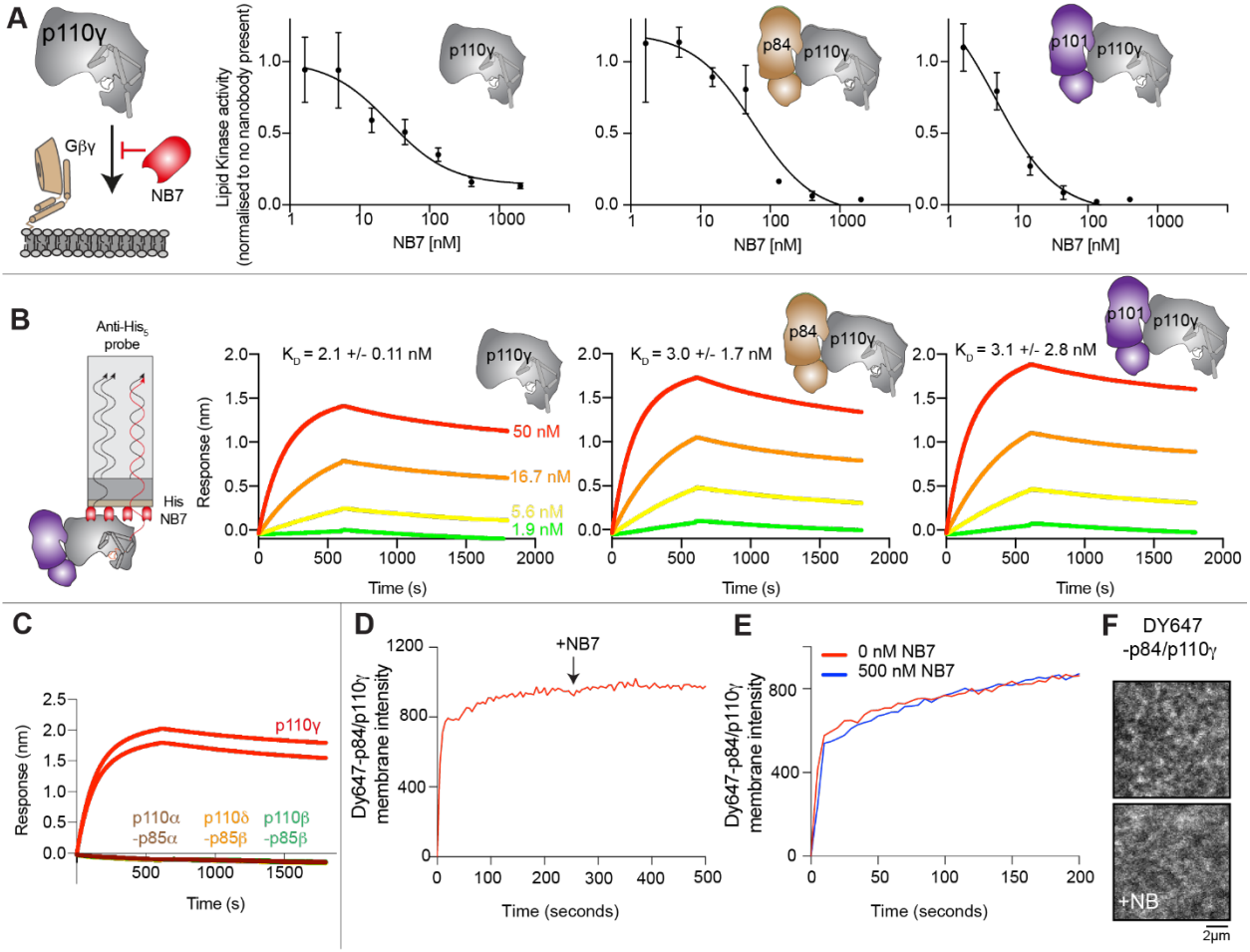

Figure 1. The inhibitory nanobody NB7 binds tightly to all p110γ complexes and inhibits kinase activity, but does not prevent membrane binding

A. Cartoon schematic depicting nanobody inhibition of activation by lipidated Gβγ (1.5 μM final concentration). Lipid kinase assays show a potent inhibition of lipid kinase activity with increasing concentrations of NB7 (3-3000 nM) for the different complexes. The protein concentration of p110γ (300 nM), p110γ-p84 (330 nM) and p110γ-p101 (12 nM) was different due to intrinsic differences of each complex to be activated by lipidated Gβγ.

B. Association and dissociation curves for the dose response of His-NB7 binding to p110γ, p110γ-p84 and p110γ-p101 (50 – 1.9 nM) is shown. A cartoon schematic of BLI analysis of the binding of immobilized His-NB7 to p110γ is shown on the left. Dissociation constants (K_D) were calculated based on a global fit to a 1:1 model for the top three concentrations and averaged with error shown.

B. Association and dissociation curves for His-NB7 binding to p110γ, p110α-p85α, p110β-p85β, and p110δ-p85β. Experiments were performed in duplicate with a final concentration of 50 nM of each class I PI3K complex.

D. Total Internal Reflection Fluorescence Microscopy (TIRF-M) analysis of the effect of nanobody NB7 on PI3K recruitment to supported lipid bilayers containing H-Ras(GTP) and farnesyl-Gβγ. Y647-p84/p110γ displays rapid equilibration kinetics and is insensitive to the addition of 500 nM nanobody (black arrow, 250 sec) on supported lipid bilayers containing H-Ras(GTP) and farnesyl-Gβγ.

E. Kinetics of 50 nM DY647-p84/p110γ membrane recruitment appears indistinguishable in the absence and presence of nanobody. Prior to sample injection, DY647-p84/p110γ was incubated for 10 minutes with 500 nM nanobody.

F. Representative TIRF-M images showing the localization of 50 nM DY647-p84/p110γ visualized in the absence or presence of 500 nM nanobody (+NB7). Membrane composition for panels C-E: 93% DOPC, 5% DOPS, 2% MCC-PE, Ras(GTP) covalently attached to MCC-PE, and 200 nM farnesyl-Gβγ.

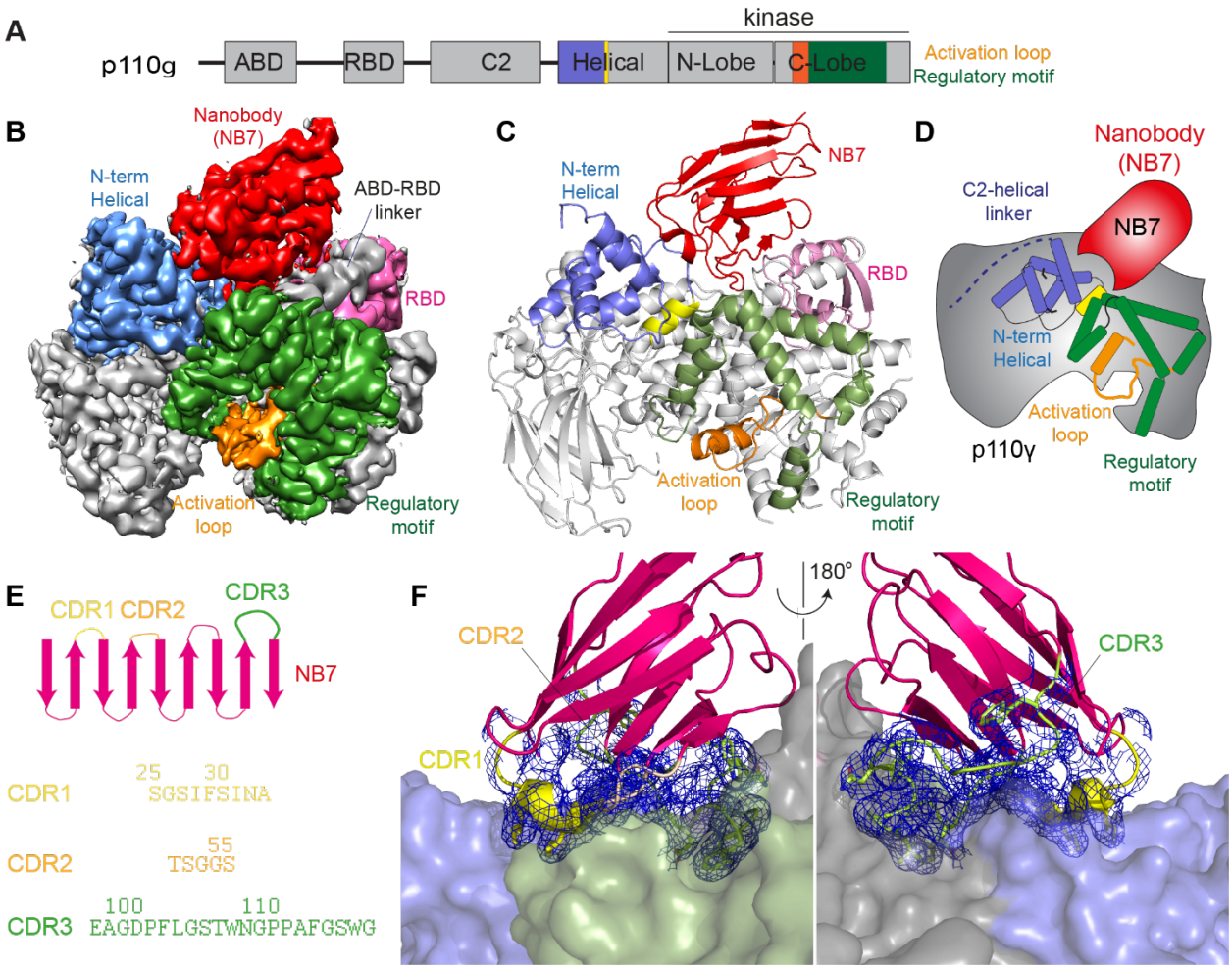

Figure 2. Structure of p110γ bound to inhibitory nanobody NB7

A. Domain schematics of p110γ with helical domain (blue), activation loop (orange), and regulatory motif (green) of p110 annotated.

B. Density map of the p110γ-NB7 complex colored according to the schematic in **A**.

C. Cartoon model of the structure of p110γ bound to NB7 colored according to **A**.

D. Schematic depicting the key features of p110 and the nanobody binding site, colored according to panel **A**.

E. Domain schematic of NB7 CDR regions and their sequences.

F. Zoom in on the binding interface of NB7, with the CDRs colored as in panel E, and the electron density of the CDR regions contoured at 3σ (blue mesh).

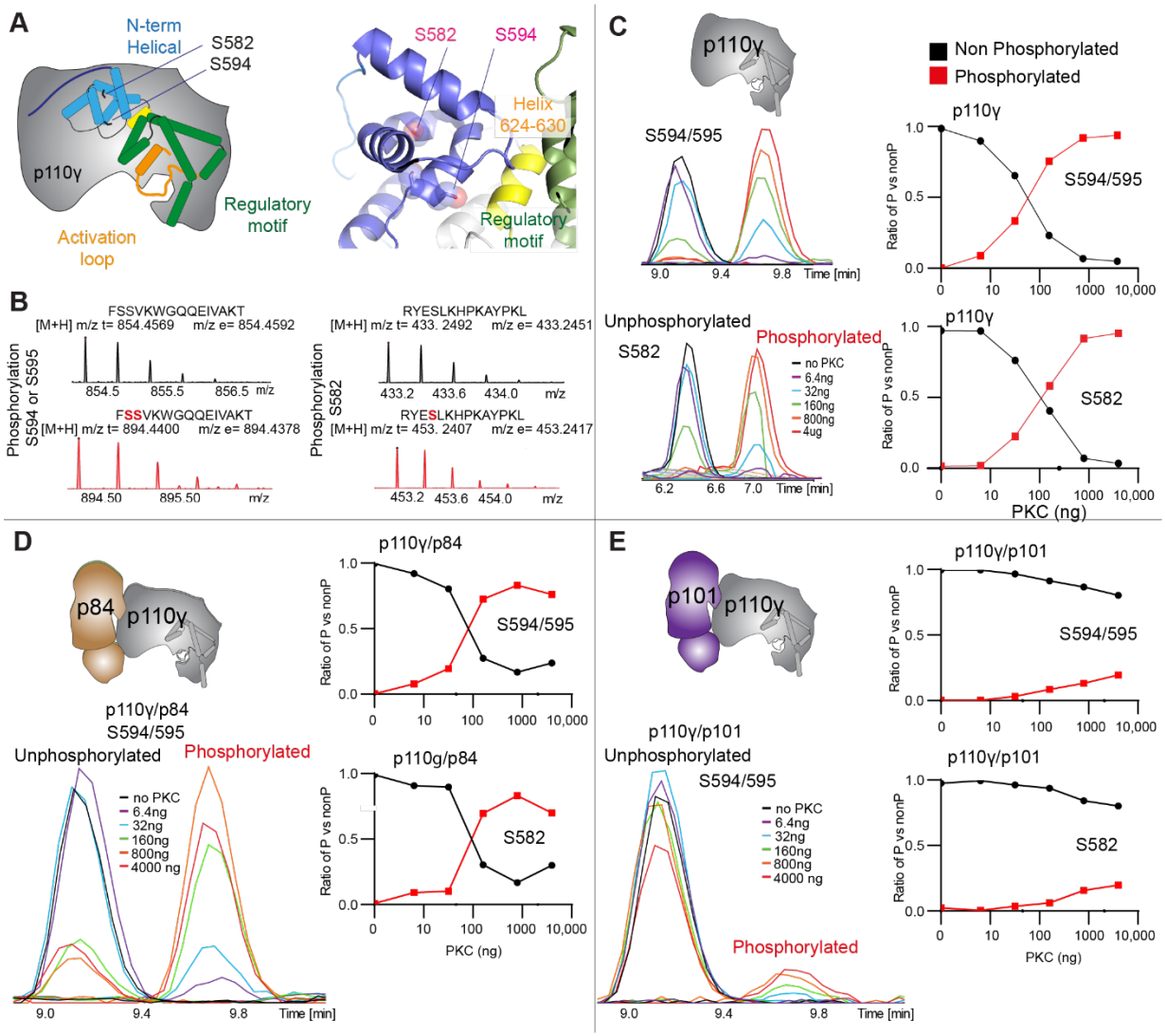

Figure 3. PKC leads to dual phosphorylation of internal sites in the helical domain, with selectivity for apo p110γ and p110γ-p84 over p110γ-p101.

A. Putative phosphorylation sites mapped on the structure of p110γ (PDB: 7MEZ) and cartoon schematic. The regions are colored based on domain schematics featured in Fig 2A.

B. Raw MS spectra of the unphosphorylated and phosphorylated peptide for a region spanning 579-592 (RYESLKHPKAYPKL) and 593-607 (FSSVKWGQQEIVAKT).

C-E. Extracted traces and ratios of the intensity of extracted ion traces of different phosphorylation site peptides (Top to bottom: S594/S595 and S582) from © p110γ, (**D**) p110γ/p84 or **(E)** p110γ/p101 samples treated with increasing concentration of PKCb according to the legend.

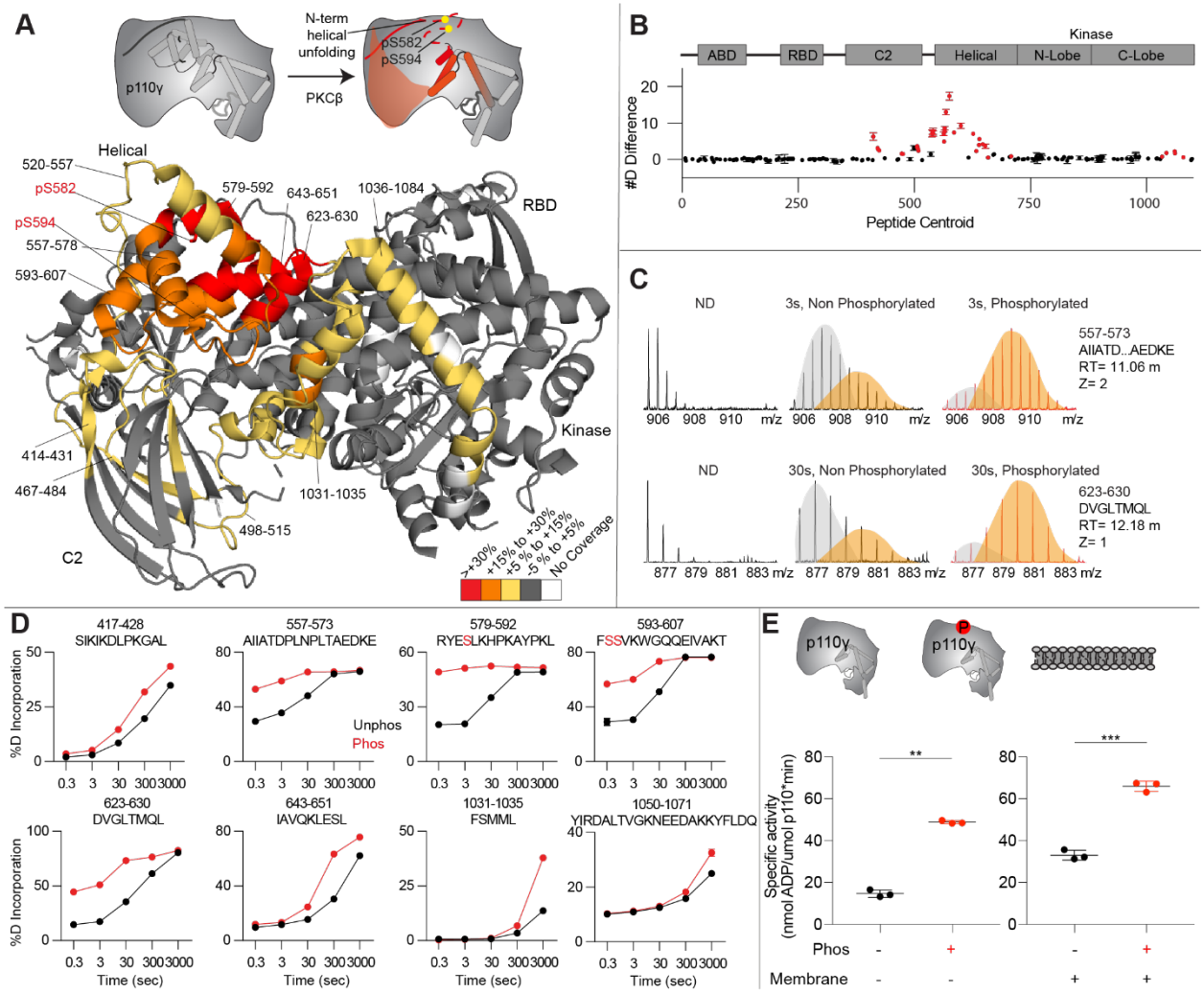

Figure 4. Activating phosphorylation at the helical domain leads to opening of the regulatory motif

A. HDX-MS comparing apo and phosphorylated p110γ. Significant differences in deuterium exchange are mapped on to the structure and cartoon of p110γ according to the legend (PDB: 7MEZ).

B. The graph of the #D difference in deuterium incorporation for p110γ, with each point representing a single peptide. Peptides colored in red are those that had a significant change in the mutants (greater than 0.4 Da and 5% difference at any timepoint, with a two tailed t-test p<0.01). Error bars are S.D. (n=3).

C. Representative bimodal distribution (EX1 kinetics) observed in the helical domain peptides of p110γ.

D. Representative p100γ peptides displaying increases in exchange in the phosphorylated state are shown. For all panels, error bars show SD (n=3)

E. Lipid kinase activity assays of phosphorylated and non-phosphorylated p100γ (concentration, 12nM to 1000nM) ATPase activity (left) and membrane (5% phosphatidylinositol 4,5-bisphosphate (PIP2), 95% phosphatidylserine (PS)) activation (right). Significance is indicated by **(<0.001%), and ***(<0.0001%).

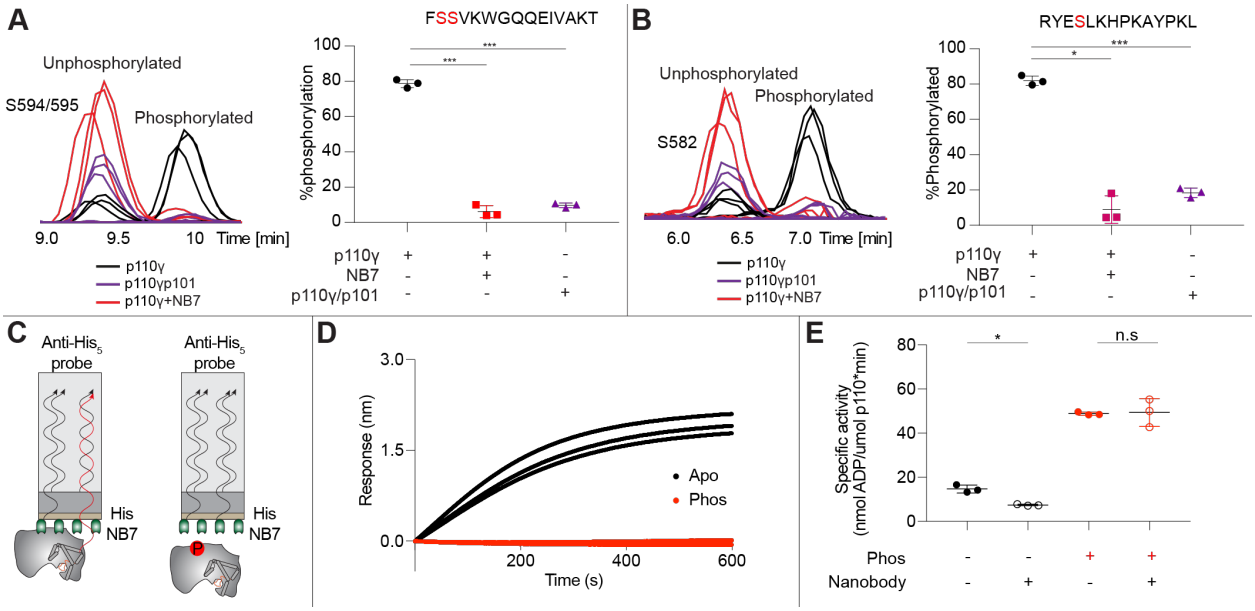

Figure 5. Nanobody NB7 blocks PKC phosphorylation, and phosphorylation prevents nanobody binding.

A. Graph showing the intensities of phosphorylated and non-phosphorylated p110γ peptide (593-607) for PKC (500 nM) treated p110γ (black), PKC treated p110γ with NB7 (red) and PKC treated p110γp101 (purple). Scatter plot showing the percent phosphorylation of each complex from the left graph for the indicated peptide (n=3, right). Significance is indicated by ***(<0.0001%).

B. Graph showing the intensities of phosphorylated and non-phosphorylated p110γ peptide (579-592) for PKC treated p110γ (black), PKC treated p110γ with NB7 (red) and PKC treated p110γp101 (purple). Scatter plot showing the percent phosphorylation of each complex from the left graph for the indicated peptide (n=3, right). Significance is indicated by * (<0.01%), and ***(<0.0001%).

C. Cartoon schematic of BLI analysis of the binding of immobilized His-NB7 to phosphorylated and non-phosphorylated p110γ.

D. Association curves for phosphorylated and non-phosphorylated p110γ (25nM) binding to His-NB7 are shown (n=3).

E. Kinase activity assays comparing the activation/inhibition of phosphorylated and non-phosphorylated p110γ (concentration, 12nM to 1000nM) with or without nanobody (3000nM final). Significance is indicated by * (<0.05%), and NS (>0.05%).

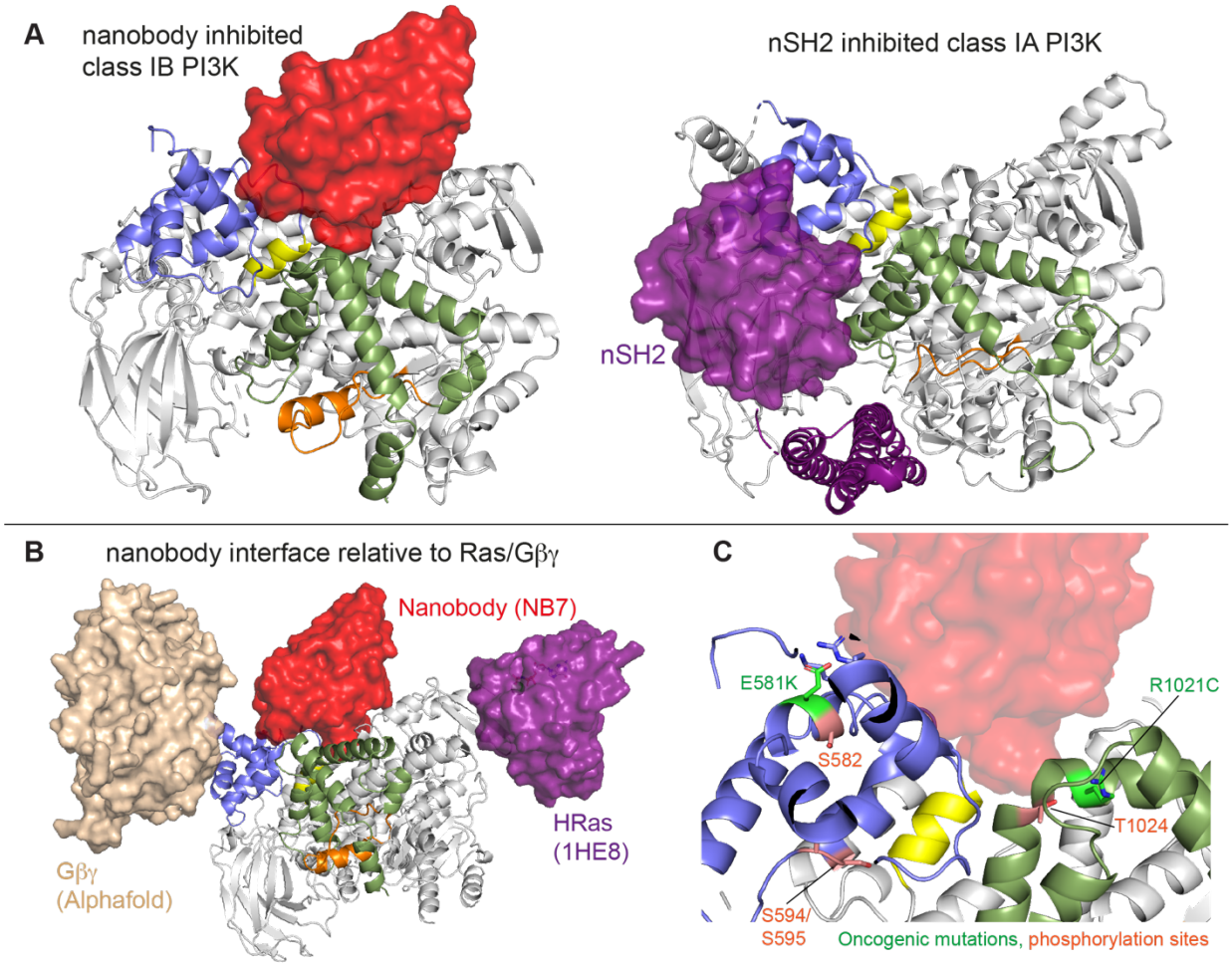

Figure 6. Comparison of nanobody binding site compared to p85 inhibition of class IA PI3Ks and class IB activation sites

A. Comparison of the nanobody NB7 binding site in p110γ compared to the nSH2 inhibitory site in p110α (PDB: 3HHM) (Mandelker et al., 2009)

B. Comparison of the nanobody NB7 binding site in p110γ compared to the X-ray structure of the Ras binding site (PDB: 1HE8) (Pacold et al., 2000) and the Alphafold model of Gβγ bound to p110γ (Rathinaswamy et al., 2023).

C. Oncogenic mutations and post-translational modifications in spatial proximity to the nanobody binding site.

Supplemental information for:

Allosteric activation or inhibition of PI3Kγ mediated through conformational changes in the p110γ helical domain

Noah J Harris[1*], Meredith L Jenkins[1*], Sung-Eun Nam, Manoj K Rathinaswamy[1], Matthew Parson[1], Harish Ranga-Prasad[1], Udit Dalwadi[2], Brandon E Moeller[1], Eleanor Sheekey[1], Scott D Hansen[3], Calvin K Yip[2%], and John E Burke[1,2%]

[1]Department of Biochemistry and Microbiology, University of Victoria, Victoria, British Columbia, V8W 2Y2, Canada

[2]Department of Biochemistry and Molecular Biology, The University of British Columbia, Vancouver, British Columbia V6T 1Z3, Canada

[3]Institute of Molecular Biology, University of Oregon, Eugene, OR 97403

*These authors contributed equally

[%]To whom correspondence should be addressed: John E. Burke

Tel: 1-250-721-8732, email: jeburke@uvic.ca

Calvin K Yip

Tel: 1-604-827-3976, em ail: calvin.yip@ubc.ca

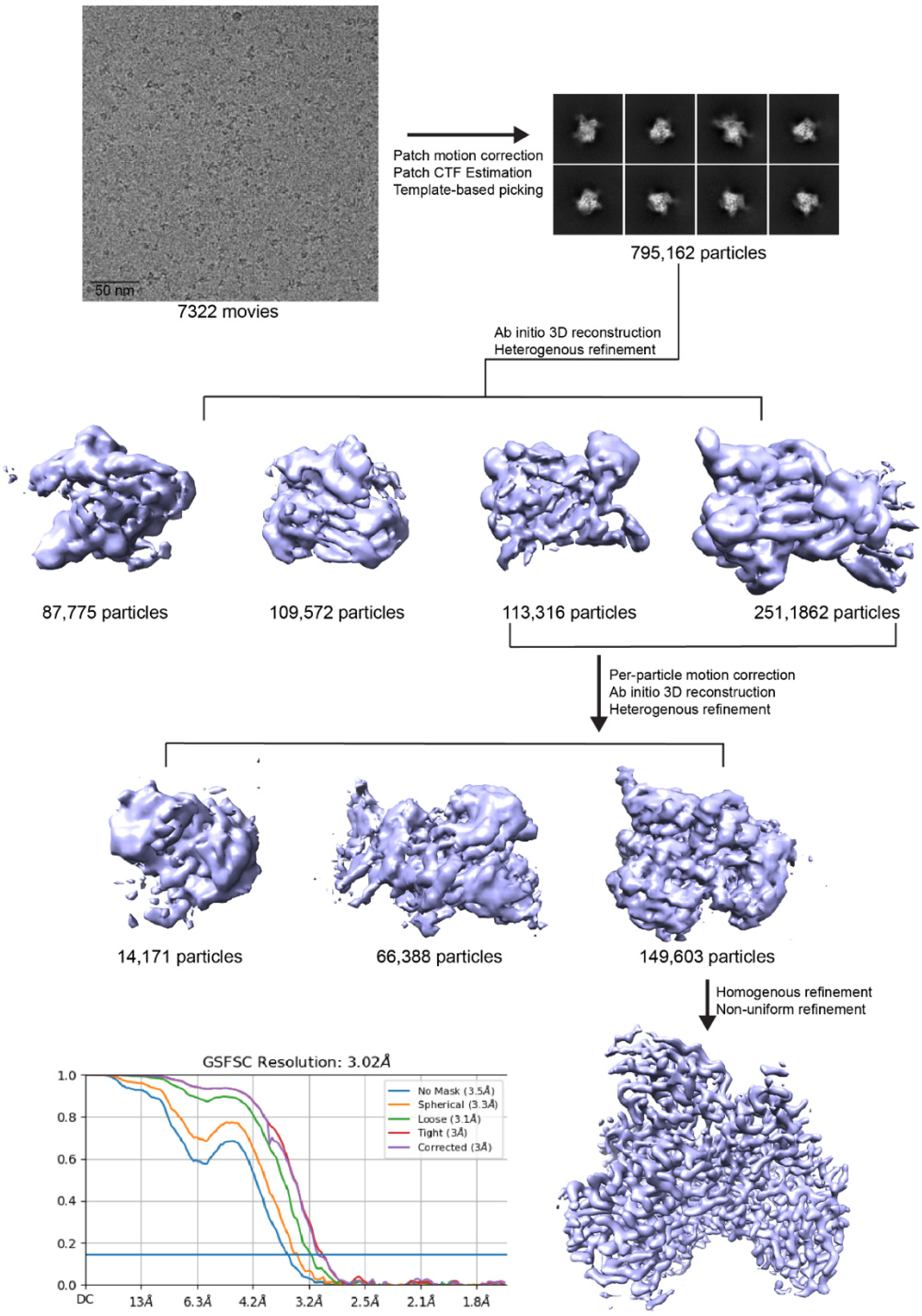

Figure S1. p110γ-NB7 complex cryo-EM analysis workflow (related to main figure 2): cryo-EM processing workflow of p110γ-NB7 complex are shown in order of a representative micrographs, representative 2D classification and 3D reconstruction processing strategy. Bottom left shows Gold-standard Fourier shell Correlation (FSC) curve of final round on non-uniform homogenous refinement.

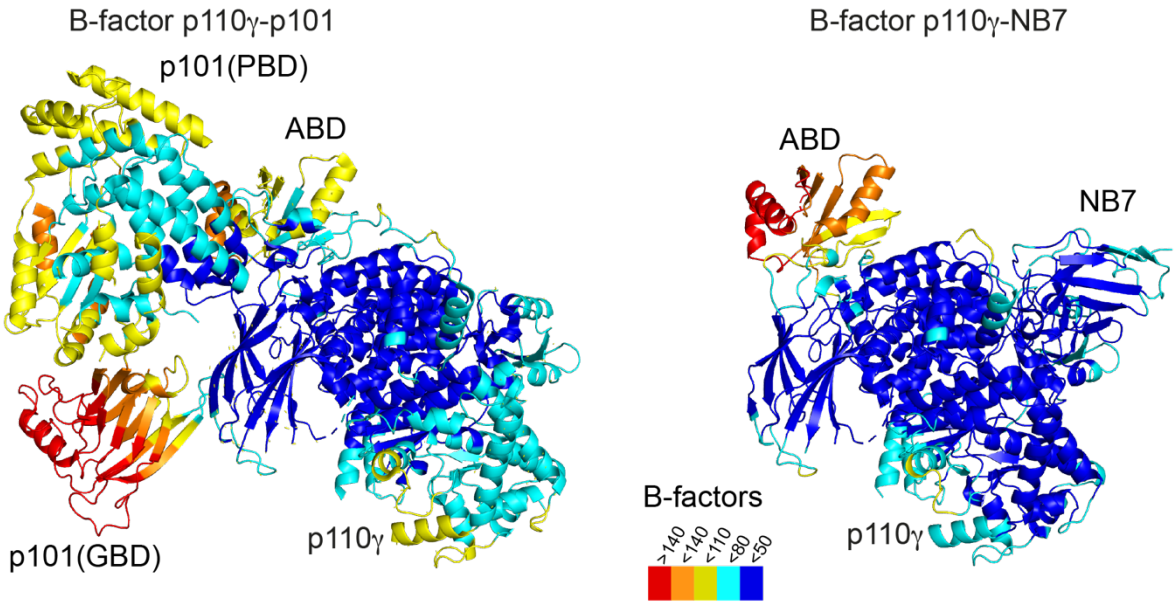

Figure S2. Comparison of full length p110γ bound to NB7 compared to p110γ-p101 (related to main figure 2): The structure of the p110γ-p101 complex (PDB:7MEZ) compared to the NB7-p110γ complex is shown colored according to B factor based on the legend.

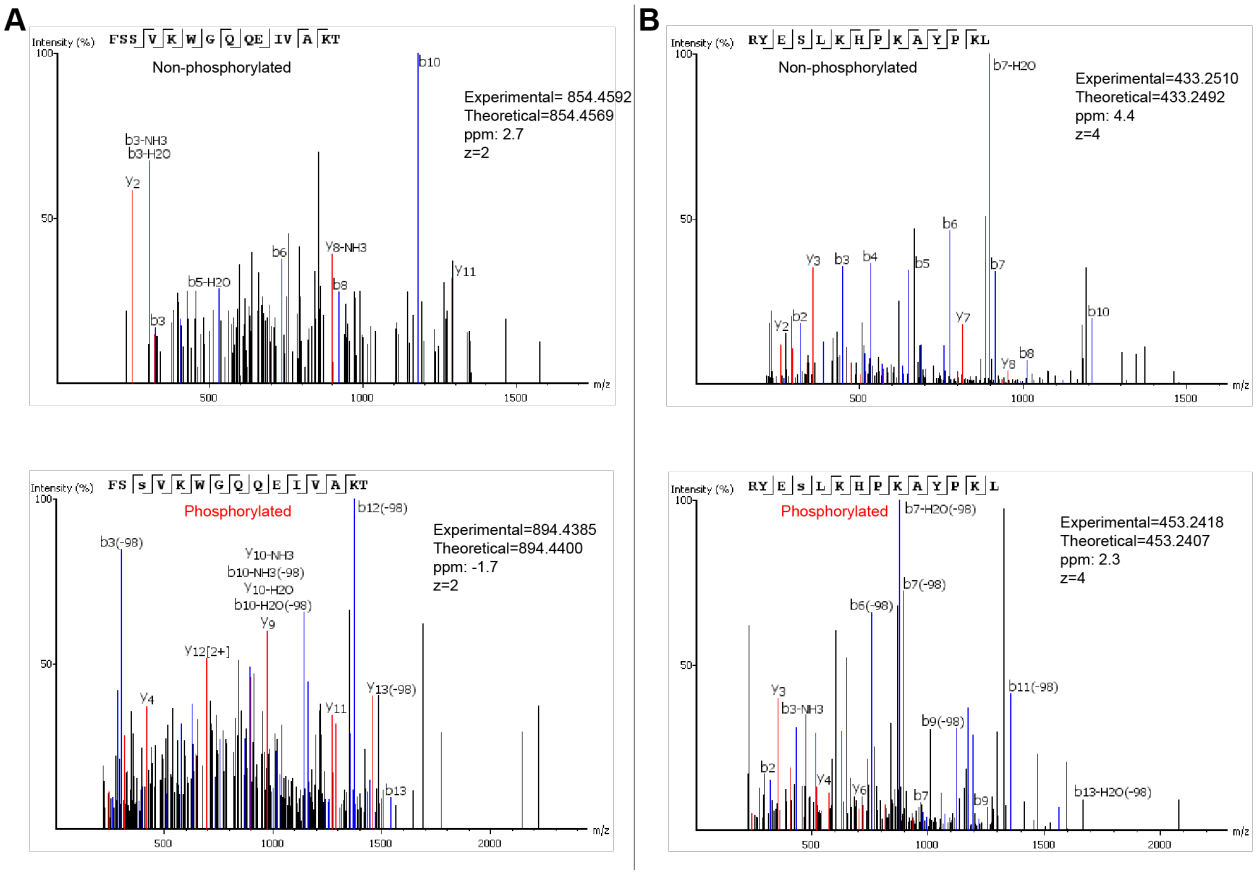

Figure S3 (related to main figure 3). MS/MS spectra of peptides spanning S582 and S594/S595 for both phosphorylated and unphosphorylated states. The theoretical and experimental mass are annotated for all peptides.

Supplementary table 1. Cryo-EM data collection, refinement and validation statistics **(related to main figure 2)**

	p110γ-NB7 EMD- 27627 PDB: 8DP0
Data collection and processing	
Magnification	
Voltage (kV)	300
Electron exposure (e/ Å^2)	50
Defocus range (nM)	500-2500
Pixel size (Å)	
Symmetry imposed	C1
Initial particle images (no.)	795,162
Final particle images (no.)	149,603
Map resolution (Å)	3.02
FSC threshold	0.143
Map resolution range (Å)	2.6-4.4
Refinement	
Initial model used (PDB)	7MEZ (p110γ only)
Model Resolution (Å)	3.02
FSC threshold	0.5
Map sharpening B factor	Sharpened locally
Model composition	
Non-hydrogen atoms	8737
Protein residues	1,066
Ligands	0
B-factors	
Protein	52.4
Validation	
Mol probability score	1.29
Clashscore	5.33
Poor rotamers (%)	0.0
Ramachandran	
Favored	98.41
Allowed	1.59
Outliers	0.0
R.m.s. deviations	
Bond lengths (Å)	0.002
Bond angles (°)	0.490
Model to map fit (CC_mask)	0.86

Supplementary table 2. HDX-MS data collection and validation statistics **(related to main figure 4)**

Data set	p110γ unphosphorylated	p110γ phosphorylated
HDX reaction details	%D_2O=75.5% $pH_{(read)}$=7.5 Temp=4ºC, 20ºC	%D_2O=75.5% pH(read)=7.5 Temp=4ºC, 20ºC
HDX time course (seconds)	3s at 4ºC, 3s, 30s, 300s, 3000s at 20 ºC	3s at 4ºC, 3s, 30s, 300s, 3000s at 20 ºC
HDX controls	N/A	N/A
Back-exchange	No correction, deuterium levels are relative	No correction, deuterium levels are relative
Number of peptides	244	244
Sequence coverage	98.4%	98.4%
Average peptide /redundancy	Length= 15.2 Redundancy= 3.3	Length= 15.2 Redundancy= 3.3
Replicates	3	3
Repeatability	Average StDev=0.53%	Average StDev=0.57%
Significant differences in HDX	>5% and >0.4 Da and unpaired t-test ≤0.01	>5% and >0.4 Da and unpaired t-test ≤0.01